2017

Hydrodynamic Measurements of the Flow Structure Emanating From A Multi-Row Film Cooling Configuration

Michael Voet
University of Central Florida

HYDRODYNAMICS MEASUREMENTS OF THE FLOW STRUCTURE EMANATING FROM A MULTI-ROW FILM COOLING CONFIGURATION

by

MICHAEL TYLER VOET
B.S. University of Central Florida, 2016

A thesis submitted in partial fulfilment of the requirements
for the degree of Master of Science
in the Department of Mechanical, Materials and Aerospace Engineering
in the College of Engineering and Computer Science
at the University of Central Florida
Orlando, Florida

Summer Term
2017

Major Professor: Jayant Kapat

ABSTRACT

The demand for more power is rapidly increasing worldwide. Attention is turned to increasing the efficiency of modern methods for power generation. Gas turbines provide 35% of the power demands within the United States. Efficiency of gas turbines is defined in an ideal sense by the thermal efficiency of the Brayton Cycle. The overall efficiency of a gas turbine can be increased while simultaneously maximizing specific work output, by increasing the turbine inlet temperature. However, even with the advancements in modern materials in terms of maximum operating temperature, various components are already subjected to temperatures higher than their melting temperatures. An increase in inlet temperature would subject various components to even higher temperatures, such that more effective cooling would be necessary, whilst ideally using the same (or less) amount of cooling air bled from compressor. Improvements in the performance of these cooling techniques is thus required. The focus of this thesis is on one such advanced cooling technique, namely film cooling.

The objective of this study is to investigate the effects of coolant density on the jet structure for different multi-row film cooling configurations. As research is performed on improving the performance of film cooling, the available conditions during testing may not reflect actual engine-like conditions. Typical operating density ratio at engine conditions are between 1.5 and 2, while it is observed that a majority of the density ratios tested in literature are between 1 and 1.5. While these tests may be executed outside of engine-like conditions, it is important to understand how density ratio effects the flow physics and film cooling performance. The density ratio within this study is varied between 1.0 and 1.5 by alternating the injecting fluid between air and Carbon Dioxide, respectively.

Both a simple cylindrical and fan-shape multi-row film cooling configuration are tested in the

present study. In order to compare the results collected from these geometries, lateral and spanwise hole-to-hole spacing, metering hole diameter, hole length, and inclination angle are held constant between all testing configurations. The effect of fluid density upon injection is examined by independently holding either blowing, momentum flux, or velocity ratio constant whilst varying density ratio. Comparisons between both of the film cooling configurations are also made as similar ratios are tested between geometries. This allows the variation in flow structure and performance to be observed from alternating the film cooling hole shape.

Particle Image Velocimetry (PIV) is implemented to obtain both streamwise and wall normal velocity measurements for the array centerline plane. This data is used to examine the interaction of the jet as it leaves the film cooling hole and the structure produced when the jet mixes with the boundary layer.

Similarities in jet to jet interactions and surface attachment between density ratios are seen for the cylindrical configuration when momentum flux ratio is held constant. When observing constant blowing ratio comparisons of the cylindrical configurations, the lower density ratio is seen to begin detaching from the wall at M = 0.72 with little evidence of coolant in the near wall region. However, the higher density cylindrical injection retains its surface attachment at M = 0.74 with noticeably more coolant near the wall, because of significantly lower momentum flux ratio and lower "jetting" effect. The fan-shape film cooling configuration demonstrates improved performance, in terms of surface attachment, over a larger range of all ratios than that of the cylindrical cases. Additionally, the fan-shape configuration is shown to constantly retain a thicker layer of low velocity fluid in the near wall region when injected with the higher density coolant, suggesting improved performance at the higher density ratio.

When tracking the jet trajectory, it is shown that the injection of CO_2 through the cylindrical configuration yields a higher centerline wall normal height per downstream location than that of the

lower density fluid. Comparing the results of the centerline tracking produced by the third and fifth rows for both the injection of air and CO_2, it is confirmed that the fifth row of injection interacts with the boundary layer at a great wall normal height than that of the third row. Additionally, when observing the change in downstream trajectory between the fifth and seventh row of injection, a significant decrease in wall normal height is seen for the coolant produced by the seventh row. It is believed that the lack of a ninth row of injection allows the coolant from the seventh row of injection to remain closer to the target surface. This is further supported by the observation of the derived pressure gradient field and the path streamlines take while interacting with the re-circulatory region produced by the injection of coolant into the boundary layer.

Further conclusions are drawn by investigating the interaction between momentum thickness and the influence of blowing ratio. Relatively constant downstream momentum thickness is observed for the injection of lower density fluid for the blowing ratio range of M = 0.4 to 0.8 for the cylindrical configuration. It is suggested that a correlation exists between momentum thickness and film cooling performance, however further studies are needed to validate this hypothesis.

For my family. I couldn't have made it here without the un-ending support and help that they provided.

ACKNOWLEDGMENTS

I would like to sincerely thank Dr. Jayant Kapat for his guidance, and the opportunity to work, learn, and grow throughout my college career.

Thank you to my CATER family for the support throughout the journey. I will always cherish those long nights spent in good company.

TABLE OF CONTENTS

LIST OF FIGURES

LIST OF TABLES

NOMENCLATURE

DR	Density ratio
I	Momentum flux ratio
M	Blowing ratio
P	Lateral pitch
u	Streamwise velocity (V_x)
v	Wall normal velocity (V_y)
V	Velocity ratio
X	Streamwise pitch

Greek

α	Inclination angle
β	Compound angle
ρ	Density
$\phi_{1,2}$	Lateral expansion angle
ϕ_3	Streamwise expansion angle
θ	Momentum thickness
$\sigma_{1,2}$	Acceptable upper and lower bound for trajectory searching

Subscript

c	Coolant (secondary)
∞	Mainstream (primary)
p	Particle

CHAPTER 1: INTRODUCTION

As today's technology advances, the ever expanding power demand is growing with it. While advances in renewable energy are happening rapidly, a majority of the power demand is met by gas turbine. Modern gas turbines operate using the Brayton Cycle, which consist of four main processes:

1 $\rightarrow$ **2** Isentropic Compression

2 $\rightarrow$ **3** Constant Pressure Combustion

3 $\rightarrow$ **4** Isentropic Expansion

4 $\rightarrow$ **1** Constant Pressure Heat Exchange

The overall efficiency of an ideal Brayton Cycle is determined by the net work of the cycle (W_{net}) and the heat put into the cycle (q_{in}), as seen in equation 1.2.

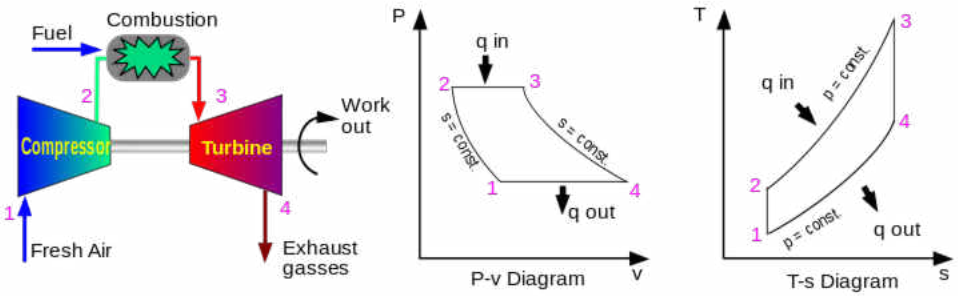

Figure 1.1: Brayton Cycle

$$W = C_P[(T_3 - T_2) - (T_4 - T_1)] \tag{1.1}$$

The work output per unit mass of the Brayton cycle can be written in terms of the temperature at the inlet and exit of the compressor and combustor, as seen in 1.1.

$$\eta = \frac{W_{net}}{q_{in}} \tag{1.2}$$

The net work can be written as the sum of the heat input and heat extracted from the cycle.

$$\eta = \frac{q_{in} - q_{out}}{q_{in}} = 1 - \frac{q_{out}}{q_{in}} \tag{1.3}$$

Recall that the heat addition and heat removal occur during a isobaric process, thus allowing the heat exchange to be expressed in terms of specific heat and temperature.

$$\eta = 1 - \frac{C_P(T_4 - T_1)}{C_P(T_3 - T_2)} \tag{1.4}$$

$$\eta = 1 - \frac{T_1}{T_3} \tag{1.5}$$

As seen in equation 1.5, the overall efficiency of an ideal Brayton Cycle is dependent on the temperature at the inlet of the compressor and the turbine entry temperature (TET).

In the early years of development, turbine manufactures were limited on the inlet temper-

ature due to material limitations. With the temperature of the gas exiting the combustor nearing the melting point of the turbine blades, the inlet temperature could not be raised without first having higher thermal resistant materials and sophisticated cooling techniques.

1.1 Gas Turbine Cooling

In the late 1960's, gas turbines had not yet began employing the use of cooling techniques. The first use of cooling came about in the late 1980's which increased the allowable gas temperature by roughly 150°C, seen in figure 1.2.

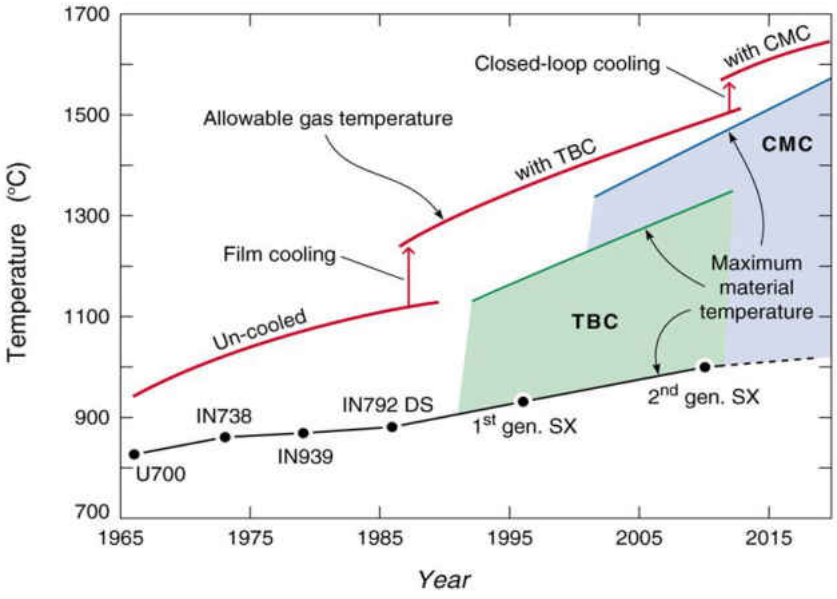

Figure 1.2: Evolution of allowable turbine gas temperature

While modern materials have advanced to accommodate these higher temperatures, without the use of secondary cooling the life span of these internal parts diminishes dramatically. To

allow these parts to survive in these high temperature environments, several different cooling techniques have been implemented. A modern day gas turbine blade and the associated cooling that have been implemented can be seen in figure 1.3. Three techniques used to protect the component from the hot gases include the use of thermal barrier coatings (not pictured), internally cooling, and externally cooling (film cooling).

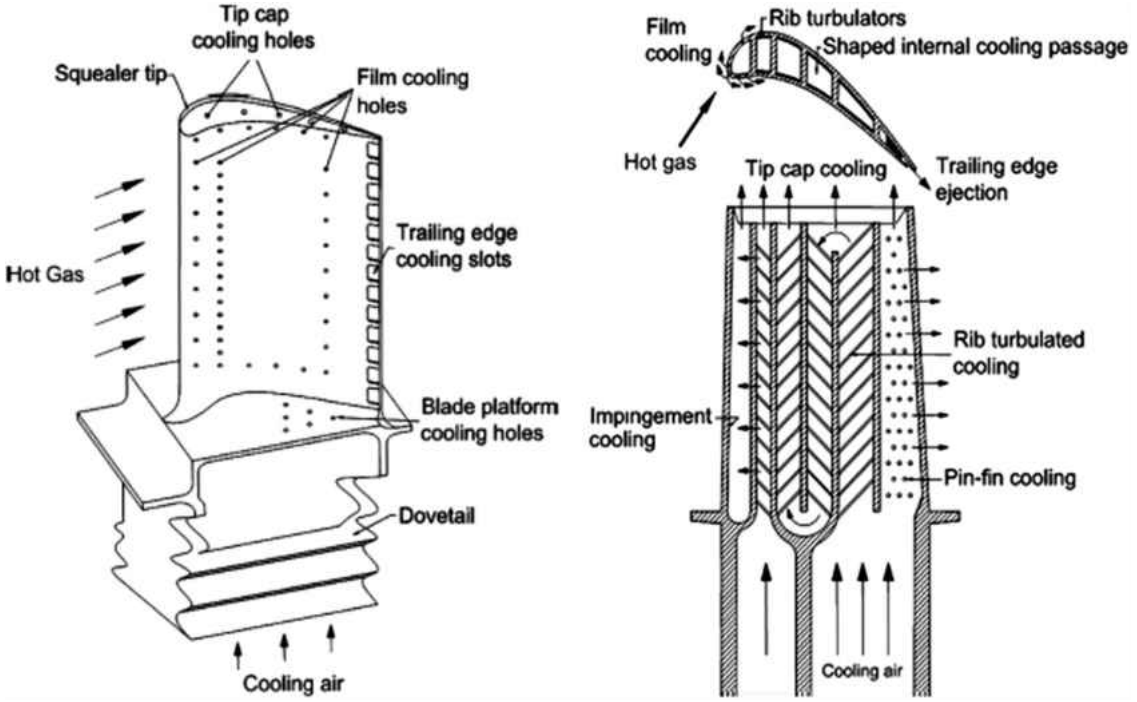

Figure 1.3: Cross section of turbine blade showing internal and external cooling

As mentioned above, in order to improve the thermal efficiency of gas turbines the turbine inlet temperature needs to increase, thereby placing larger thermal loads on the internal components. In order to increase the turbine inlet temperature the cooling of the internal components must also sufficiently increase. Currently 20 to 30 percent of the flow from the compressor is required to adequately cool the engine [1]. Ideally the increase in turbine cooling performance

would not require any additional flow from the compressor, while potentially even reducing the amount of air bled from the compressor. In the fight against the increasing turbine inlet temperature, film cooling has been call ”the first and best line of defense for hot gas path surfaces against the onslaught of extreme heat fluxes” [2].

1.1.1 Film Cooling

> ”The art and science of film cooling concerns the bleeding of internal component cooling air through the external walls to form a protective layer of cooling between the hot gases and the component external surfaces.” -Bunker [2]

The research into film cooling began with the application in reentry vehicles and surfaces exposed to plasma jets, rockets, or flame tube devices [2]. In these applications, the film are typically introduced via a two-dimensional tangential slot. However, slot cooling is not used on the high pressure turbine blades due to high stress concentrations associated with slots, ultimately reducing the blades structural integrity. As an alternative, discrete holes are used with the goal of replicating the ideal film created by a continuous slot. [2].

Hole shape plays a crucial role in the performance of the film produced by the jet. In the early stages of use, film cooling holes were employed as simple cylindrical holes. First seen in military, follow by commercial engines, was the introduction of a lateral expansion angle ($\phi_{1,2}$) into the exit of film cooling holes [2]. Several additional geometric parameters are employed in film cooling and are introduced below.

Hole Diameter, D - The diameter of the hole to which the coolant is supplied to the testing surface, also referred to as metering diameter.

Hole Length, L - The overall length of the passage that coolant is supplied to the testing

surface, typically written in terms of hole diameter as L/D. The length of the hole plays a crucial role in the development and delivery of the secondary flow between the coolant passage and testing surface. Short hole lengths (L/D $<$4) do not allow the coolant to relax from the disturbance produced by entrance and ultimately produce a more pronounced jetting effect. By increasing the hole length (L/D $>$4), the coolant is allowed more length to develop characteristics of pipe flow, typically resulting in a more uniform velocity profile upon injection reducing the penetration of the coolant [3].

Inclination Angle, α - The streamwise angle between the wall and axis of the film cooling hole. The primary purpose of inclination angle is to reduce the vertical component of the coolant momentum as is exits the film cooling hole. As inclination angle decreases, the formation of a separation bubble develops on the downstream wall of the film cooling hole.

Compound Angle, β - The angle relative to the flow based on the axis projected in the wall normal direction. Typically the angle is in the range of $\pm$ 90°. By laterally angling the injection of the coolant relative to the flow, the wall normal velocity component is thereby reduced while additionally prompting lateral spreading.

Lateral Expansion Angle, $\phi_{1,2}$ - By laterally expanding the area of the hole just prior to injection the jet velocity is reduced while increasing the lateral coverage of the coolant, thereby increasing coverage, surface attachment, and efficiency.

Laidback Angle, ϕ_3 - In addition to lateral expansion, the area of the film cooling hole can also be expanded in the streamwise direction. With this streamwise expansion, effective area of the coolant is increased further reducing the velocity upon injection while also reducing the angle of injection as the coolant entering the boundary layer.

While there are numerous advancements that can be made to improve the coverage of

film cooling holes, effectively testing these improvements in an environment similar to engine like conditions is crucial to accurately evaluate performance. Classifying film cooling conditions is accomplished using a series of ratios between the primary and secondary flow. These ratios involve the use of the primary flow bulk velocity and density, accompanied by the secondary flow bulk velocity and density. Typical non-geometric parameters used in film cooling are defined as such:

Mass Flux Ratio, (M)

$$M = \frac{(u_c)(\rho_c)}{(u_\infty)(\rho_\infty)} = (DR)(V) \tag{1.6}$$

Mass flux ratio , commonly referred to as blowing ratio, is a ratio of the cool secondary mass flux to the hot primary mass flux. This ratio portrays the mass addition to the boundary layer by the secondary flow, and is a function of the velocity and density of both the primary and secondary flow. Blowing ratio can be re-written as a function of density ratio and velocity ratio, which are defined below.

Momentum Flux Ratio, (I)

$$I = \frac{(u_c)^2(\rho_c)}{(u_\infty)^2(\rho_\infty)} = (DR)(V^2) \tag{1.7}$$

Momentum flux ratio describes the ratio of the secondary (coolant) momentum to the primary (freestream) momentum.

Velocity Ratio, (V)

$$V = \frac{u_c}{u_\infty} \tag{1.8}$$

Velocity ratio is a function of only the bulk primary velocity and coolant velocity. The coolant velocity used in velocity ratio is determined by the diameter of the film cooling hole.

Density Ratio, (DR)

$$DR = \frac{\rho_c}{\rho_\infty} \tag{1.9}$$

The effect of density ratio are particularly interesting to researchers. Density ratios during typical engine operation are in the range of 1.5 to 2.0 [4]. However, the typical range of density ratios evaluated through out literature is in the range of 1 and 1.5. The effective density ratio used during the time of testing for a particular film cooling configuration ultimately is determined by the availability and practicality of achieving a particular density ratio, and the experimental technique implemented during testing.

Pietrzyk describes three ways to achieve a particular density ratio as to heat the primary flow, cryogenically cool the secondary flow, or the use of a foreign gas as the secondary fluid [5]. Also, the method of achieving a particular density ratio can eliminate the possibility of using certain testing techniques. For example, "Experiments using a hot free-stream flow or using foreign gas injection do not lend themselves to hot-wire investigations" [5].

1.2 Literature Review

1.2.1 Computational Studies

T. Kampe (2012)

Kampe *et al.* [3] compared the effects of inclination angle and length-to-diameter ratio on the flow structure produced by a cylindrical film cooling hole. Using ANSYS CFX 12, a single discrete film

cooling hole was modeled with inclination angles of 60° and 40°. Additionally, the 40° inclination angle is modeled with length-to-diameter ratios (L/D) of 4 and 10 to demonstrate the effects of increased entrance length prior to injection.

For a short length-to-diameter ratio of L/D = 4 at an inclindation angle of 40°, the separation region developed as the coolant enters the film cooling hole is observed to extend beyond the hole exit due to the lack of length required to allow the flow features to relax [3]. However, the additional length gain with an L/D = 10 allowed the flow features to settle prior to injection, eliminating the presence of the separation bubble at the hole exit. The increased entrance length produced a more uniform velocity profile as a result of the additional mixing gained over that of the shorter length. An increased length-to-diameter ratio thereby reduces the penetration of the jet into the crossflow when compared to the shorter L/D.

J. Hossain (2014,2017)

Hossain *et al.* [6] [7] compared the results obtained from both a numerical and experimental investigation into a single row impingement channel. Impingement jets with a hole diameter of 7.5mm are investigated at Reynolds numbers of 15,000 and 30,000. Experimental techniques used during these studies include Temperature Sensitive Paint (TSP) and Particle Image Velocimetry (PIV). Using StarCCM+, both RANS and LES prediction models are solved for the testing configuration.

Particle Image Velocimetry and Temperature Sensitive Paint are compared to the results calculated by a $v^2 - f$ turbulence model simulation [6]. Wall static pressure and local mass flux distributions show good agreement between experimental and numerical findings. However, comparison of the spanwise averaged Nusselt number between computational and experimental results shows that CFD over predicts the heat transfer expected. Additionally, when compared with the flowfield results, the crossflow magnitude was shown to be under predicted by the computation

modeling.

An additional study was preformed comparing several computation methods, including RANS and LES, to experimental results [7]. In comparison to the results obtained with the RANS models, the Large Eddy Simulation (LES) model shows great agreement with both the experimentally obtained flowfield and heat transfer results.

1.2.2 Single Row Film Cooling

R. J. Goldstein (1974)

Goldstein and Eckert [8] performed both flow visualization and effectiveness measurements on three hole shapes for a single row of eleven holes inclined at 35°. The three hole shapes used in the study included a fan shaped hole laterally expanded at 10° in both direction and two simple cylindrical holes of varying hole length. The holes were 6.35 mm in diameter with a hole-to-hole spacing of P/D = 3. The freestream velocity is varied from 20 to 55m/s and is maintained at room temperature. The density ratio was varied by alternating the secondary fluid between air and refrigerant-12, yielding density ratios of ρ = 1.0 and 3.5 respectively. The blowing ratios tested within the study vary between M = 0.52 and 2.20.

The effect of film cooling hole length was observed to produce ”no appreciable difference” when comparing the results of the long and short lengths tested [8]. Increased effectiveness was seen for the laterally expanded holes immediately downstream of injection when compared with the simple cylindrical holes. Additionally, the shaped film cooling holes were more successful in spreading the coolant laterally than that of the cylindrical holes. It is believed that the increased area gained from the lateral expansion of the holes allowed the velocity of the coolant to decrease upon injection, thereby lowering the effective blowing ratio allowing the jet to remain

closer to the wall. With the use of refrigerant-12, increased surface effectiveness was observed for higher blowing ratios than that of air injection.

J. R. Pietrzyk (1990)

Pietrzyk *et al.* [5] researches the effects of density ratio on a single row of eleven holes simple cylindrical holes inclined at 35° within a closed loop wind tunnel. The simple cylindrical holes tested had a diameter of 12.7mm with lateral hole-to-hole spacings of P/D = 3, and a short hole length of L/D = 3.5. The freestream velocity was maintained at 20 m/s with a turbulence intensity of 0.2%. Using a water-cooled heat exchanger, the freestream temperature was kept at 302K throughout testing. Using liquid Nitrogen to cryogencially cool the secondary flow such that the jet temperature is maintained at 153K, resulting in a density ratio of 2.0. Accompanying this work is data presented in a previous study citeref23 where a density ratio of 1.0 is tested. One mass flux ratio is tested at M = 0.5 at the high density ratio of 2.0 and compared to the previous work done at the unity density ratio of 1.0. The resulting momentum flux ratios are I = 0.125 achieved from DR = 2.0, accompanied by I = 0.062 and 0.25 from the previous study using DR = 1.0. Laser-doppler velocimetry (LDV) was used to obtain streamwise contours along the centerline of the hole.

In the region near the hole exit, there was similarities in mean velocity contours between the high density and low density jets when velocity ratio is constant. Upon moving downstream, beyond x/D = 15, similarities between jet densities shift. In this downstream region, the velocity profiles between the high and low density jets have great similarity when mass flux is held constant.

When comparing magnitudes of turbulent shear stress, it was determined that the development of these stresses are due to the local velocity gradient at the hole exit [5]. While the levels of turbulence intensity for all three cases examined are comparable in magnitude, it was shown that the higher density jet retained elevated levels of turbulence intensity for greater downstream

distances than those of the unity density cases.

Stefan Bernsdorf (2006)

Berbsdorf *et al.* [9] evaluates the effects of inclination angle on a row of seven simple cylindrical holes inclined at 30° and 50° within a closed loop wind tunnel. Density ratio is varied by heating the primary flow and cooling the secondary flow, with an effective density ratio range of 1.0 - 1.6. The blowing ratios test are between 1.0 and 2.0. Streamwise, spanwise, and wall parallel flowfield measurements are captured using stereo particle image velocimetry, providing incite for all three velocity components. The effects of varying blowing ratio, density ratio, and inclination angle on the wall normal height location and strength of the kidney vortex pair are discussed.

Spanwise stereo planes are used to evaluate the effect of density ratio on the counter rotating vortex that develops downstream of coolant injection. When comparing density ratio, the higher density fluid was noted to have a weaker jet than the lower density ratio at a fixed blowing ratio. The center of the counter rotating vortex pair (CVPs) is observed to be closer to the wall for the higher density ratio, and ”entrain more low velocity fluid into the centre of the jets than the corresponding low DR case” [9]. An increase in inclination angle is shown to increase the wall normal height of the center of the jet for a given blowing ratio, however the center of the CVPs decreases with increasing inclination angle. Additionally, the increase in inclination angle dramatically increases the influence of the CVPs as well as the entrainment of low velocity fluid.

Blake Johnson (2013)

Johnson *et al.* [10] studied the effects of density ratio on a single row containing three simple cylindrical holes inclined at 30°. Nitrogen, Air, and Carbon Dioxide, are used as the secondary

fluid to achieve density ratios of 0.97, 1.00, and 1.53 respectively. The effective blowing ratios tested in this study are 0.85 and 1.70 Using particle image velocimetry and pressure sensitive paint, streamwise flowfield and surface effectiveness measurements are obtained for fixed values of blowing ratio, momentum flux ratio, and velocity ratio while density ratio is varied [10].

Jet separation was observed at a blowing ratio of M = 1.70 for the density ratio DR = 1.0, however the higher density ratio of DR = 1.53 remained attached to the surface for the same blowing ratio. In terms of surface effectiveness, the higher density ratio of DR = 1.53 is shown to have better performance than the lower density ratio of DR = 0.97 for the constant blowing ratio comparison of M = 0.85 and 1.70. Constant momentum flux and constant velocity ratio comparisons are additionally made in terms of surface effectiveness for alternating density ratio. At low blowing and momentum flux ratios (M $<$0.4 and I $<$0.17), density ratio had little variation on surface effectiveness. For the larger blowing and momentum flux ratio comparisons of M = 0.85 and 1.70, and I = 0.46 and I = 0.94, the higher density ratio is seen to produce elevated surface effectiveness than that of the lower density ratio. In the case of constant velocity ratio comparisons, good agreement was seen between the low and high density ratios at V = 0.88.

Peter Schreivogel (2014)

Schreivogel *et al.* [11] evaluates the effects of density ratio on the flow structure of a single row of both a simple cylindrical and trenched cylindrical hole inclined at 30° within a closed loop wind tunnel. Using liquid nitrogen to cool the secondary flow while the temperature of the primary flow is held constant, density ratios of 1.33, 1.6, and 2.0 are tested for both hole types. Particle image velocimety was used to acquire various streamwise and wall parallel flow field planes. Density ratio is varied as either blowing ratio, momentum flux ratio, or velocity ratio is held constant.

It was determined that the jet trajectory was best scaled with momentum flux ratio as

density ratio was varied, while mixing was influenced on velocity differences between the primary and secondary fluids upon injection.

Molly Eberly (2014)

Eberly *et al.* [12] investigates the density ratio effects on a single row of five simple cylindrical holes inclined at 30° within a closed loop wind tunnel. Liquid nitrogen is used to cool the secondary flow while a heater is used to elevate the temperature of the primary flow. The effective density ratios tested are 1.0, 1.2, and 1.6. Streamwise planes are taken at the centerline and hole edge using time-resolved particle image velocimetry.

Turbulence levels were found to scale with momentum flux ratio where a momentum flux of one yielded the lowest turbulence intensity. However, a blowing ratio of one was found to yield the lowest magnitude of turbulence intensity in the shear layer due to the matching mass flux between the primary and secondary flow.

Travis B. Watson (2016)

Watson *et al.* [13] evaluates the flow structures and surface effectiveness of a single row inclined at 30° for a simple cylindrical and laidback fan-shape hole within an open loop wind tunnel. Four density ratios of DR = 1, 2, 3, and 4 are tested throughout this study. Air is used as the secondary fluid for the DR = 1, while a combination of argon and sulfur hexafluoride (SF_6) is used for DR = 2, 3, and 4. The low speed primary flow is maintained at 10 m/s. Three blowing ratio are tested in this study of M = 0.5, 1.0, and 1.5. Surface effectiveness measurements are obtained by use of the Pressure Sensitive Paint (PSP) technique. Stereoscopic-Particle Image Velocimetry is used to evaluate spanwise planes at various locations downstream of the injection.

Surface effectiveness measurements show that as density ratio is increased, the lateral spreading of the jet immediately downstream of injection is enhanced due to the decrease in momentum associated with the slowed coolant. At low blowing ratios, the increased lateral spreading associated with increasing density ratio expedites mixing thereby reducing the effectiveness in the downstream region. However, at an elevated blowing ratio of M = 1.5, the jet wants to lift off the surface. Increases in density ratio at elevated blowing ratios continue to reduce the injection momentum allowing increased surface effectiveness downstream of injection.

1.2.3 Multi-Row Film Cooling

Mark K. Harrington (2001)

Harrington *et al.* [14] investigates the adiabatic effectiveness by the use of infrared technology of both a single row and ten consecutive staggered rows of wall normal (90°) holes within a closed loop wind tunnel. The holes studied were 6mm in diameter and had hole spacings of P/D = 7.14 and X/D = 7.14. The freestream velocity was maintained at a 10 m/s, while the freestream turbulence intensity was varied between 0.5% and 18% by utilizing an upstream turbulence generator. With the use of liquid nitrogen, the secondary flow was cooled as low as -90°C yielding a density ratio of 1.7. The blowing ratio was varied between M = 0.25 and M = 1.0, resulting in momentum flux ratios between I = 0.04 and I = 0.59. Computational fluid dynamics is also performed for blowing ratios M = 0.25 and M = 0.65, with low freestream turbulence intensity modeled using a RNG k - ϵ approach.

Findings suggest that eight rows of holes were required to establish ”an asymptotic ’full developed’ adiabatic effectiveness level” [14]. Maximum surface effectiveness was seen at a blowing ratio of M = 0.65, with marginal changes in effectiveness as the blowing ratio was increased

to M = 1.0. Elevated levels of freestream turbulence intensity showed a decrease in effectiveness for the M = 0.25 case by 30%, while at higher blowing ratios of M = 0.65 and M = 1.0, a 14% reduction in effectiveness was observed. It is believed that the combination of jet separation due to high blowing ratio and elevated freestream turbulence levels allowed for increased dispersion of coolant, aiding in surface coverage. Superposition techniques used to predict surface effectiveness both by measurements and CFD are seen to over predict surface effectiveness when compared to experimental data.

Wilhelm Jessen (2012)

Jessen *et al.* [15] studies the flowfield produced by three staggered rows of thirteen laidback-fan shaped holes inclined at α = 30° with a lateral expansion of ϕ = 10° and laidback of γ = 8° within a closed loop wind tunnel. The film cooling holes have a diameter of 10mm with hole-to-hole spacings of P/D = 3 and X/D = 6. The effect of an adverse pressure gradient is examined; the adverse pressure gradient is induced via a contoured wall opposite the location of injection. The secondary fluid is alternated between air and carbon dioxide, producing density ratios of 1.0 and 1.53, respectively. The blowing ratio is altered between M = 0.28 and 0.48, producing momentum flux ratios between I = 0.05 and 0.23.

Both two and three component particle image velocimetry are used to examine the flow field normal to the wall. For the zero pressure gradient case, the boundary layer is observed to grow with each row of injection. With the boundary layer thickness increased due to the prior rows' injection, the jet penetrates further into the freestream. As a result, a decrease in the wall-normal velocity gradient is seen along with an enlarged mixing region [15]. The presence of a pressure gradient in the freestream was shown to amplify these results. Additionally, the freestream velocity is reduced in the region of the pressure gradient, thereby allowing the jet to lift further

off the surface. It was concluded that elevated levels of turbulence are seen in the shear layer for the higher density injection, suggesting that increased mixing ultimately leading to decreased efficiency [15].

Table 1.1: Film cooling literature

Year	Data	Rows	α	$\phi_{1,2}$	ϕ_3	D [mm]	L/D	P/D	X/D	Citation
1974		1	35°	0, 10°	0°	6.35	5.2	3	0	Goldstein [8]
1990	PIV, CFD	1	35°	0°	0°	6	5.2	4.55	0	Schreivogel [11]
2006	PIV	1	30, 50°	0°	0°	5	2.8	4	0	Bernsdorf [9]
2012	PIV	3	30°	10°	8°	10	24	3	6	Jessen [15]
2012	CFD	1	40, 60°	0°	0°		4, 10	0	0	Kampe [3]
2013	PIV, PSP	1	30°	0°	0°	5	6	10	0	Johnson [10]
2014	PIV	1	30°	0°	0°	8.2	4.7	3	0	Eberly [12]
2016	PIV, PSP	1	30°	0, 10°	0,10°	4.76	4, 6	5	0	Watson [13]
2017	PIV	8	20°	0, 14°	0°	3.81	11.2	7.5	7.5	Present Study

CHAPTER 2: EXPERIMENTAL SETUP

2.1 Film Cooling Configurations

In the present study, two film cooling configurations are examined; a simple cylindrical and a ϕ = 10° laterally expanded hole, seen in figure 2.1. Simple cylindrical film cooling configurations are well documented throughout literature and while the inclination angle of 20°chosen for this study is not widely tested, the ability to compare with the wide range of available data is beneficial. Additionally, the data presented in this study can provide validation to future computational fluid dynamics (CFD). As previously discussed, by expanding the exit of the film cooling hole laterally relative to the flow prior to injection, the area is increased prior to injection and thereby lowering the velocity of the coolant. This laterally expanded hole, also referred to as a fan-shape or diffuser, offers improved performance over traditional simple cylindrical holes as the coolant downstream effectively covers a greater lateral area while retaining improved surface attachment. Through testing of both a simple cylindrical and laterally expanded film cooling configuration, a complete view of the variations in the flow field by altering the injection shape can be examined.

The cylindrical configuration was manufactured via machining into an aluminum plate. Due the complexity in the hole shape when compared to the simple cylindrical configuration, the fan-shaped geometry was manufactured via Stereolithography (SLA). Each of the manufactured geometries, referred to as coupons, were designed such that they can easily be swapped into the wind tunnel for testing. Each of these coupons have an overall dimension of 375.65 mm wide by 450.85 mm long (direction parallel to flow) and can be seen in figure 2.2 and figure 2.3. A 10 mm flange boarders the edges of the coupon and are used for sealing purposes.

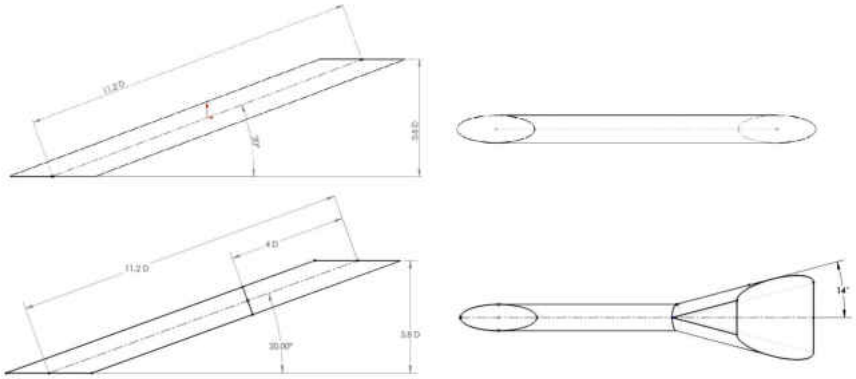

Figure 2.1: Cylindrical hole (top) and fan-shape hole (bottom)

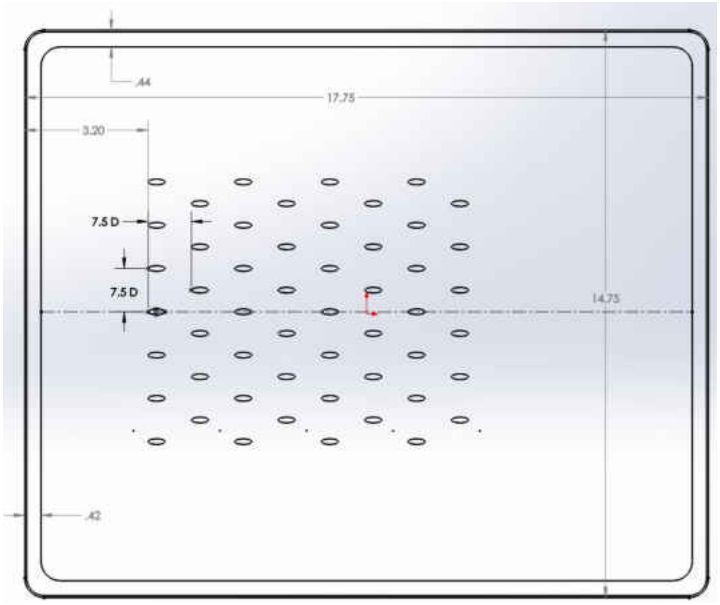

Figure 2.2: Cylindrical configuration

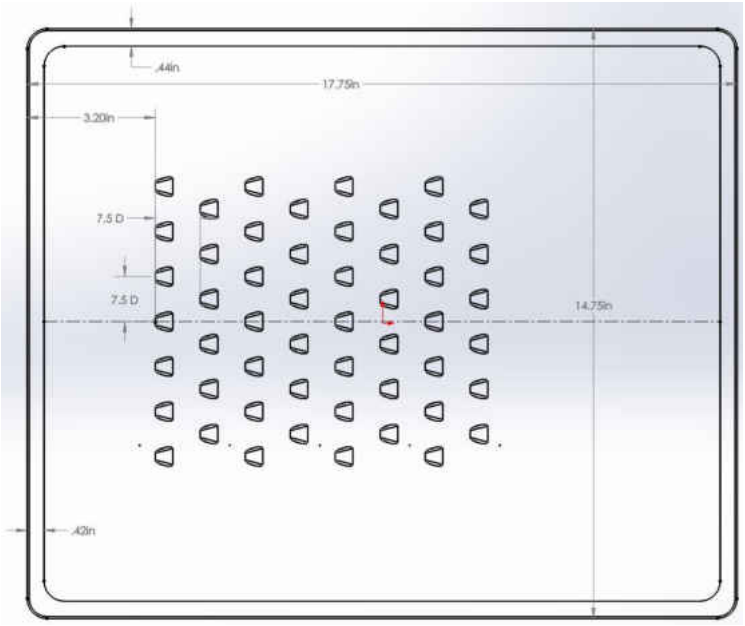

Figure 2.3: Fan-shaped configuration

Both geometries consist of eight rows in a straggled arrangement alternating between seven and six holes per row, resulting in a total of 52 holes. The lateral and a streamwise pitch-to-hole-diameter ratio of P/D = X/D = 7.5 is consistent between both of the geometries. Seen in tables 2.1 and 2.2 are the nominal and measured hole geometry parameters. Each of the holes is 3.81 mm in diameter and have a length-to-hole-diameter ratio of L/D = 11.2.

Reflections are a major concern when performing PIV, as they can damage equipment, potentially harm bystanders, and also contaminate data (as discussed in future section). In order to attempt to reduce the potential and magnitude of anticipated reflections, each of the testing coupons is painted using flat black spray paint. It is assumed that the thickness of the paint added is negligible.

Table 2.1: Test matrix with nominal parameters

Geo Num	Hole Type	Hole Diameter	Angle	Total length	Lat. pitch	Axial pitch	Material
		d (mils)	α (°)	$(L+L')/d$	P_z/d	P_x/d	
1	Cylindrical	150	20	11.2	7.5	7.5	Al
5	Diffuser	150	20	11.2	7.5	7.5	SLA

Table 2.2: Test matrix with actual measured parameters

Geo Num	Hole Type	Hole Diameter	Angle	Total length	Lat. pitch	Axial pitch	Material
		d (mils)	α (°)	$(L+L')/d$	P_z/d	P_x/d	
1	Cylindrical	144.2 ± 1.6	20	11.7 ± 1.4	7.8 ± 0.1	7.7 ± 0.1	Al
5	Diffuser	144.4 ± 2.7	20	11.8 ± 1.4	8.0 ± 0.3	7.8 ± 0.2	SLA

2.2 Wind Tunnel

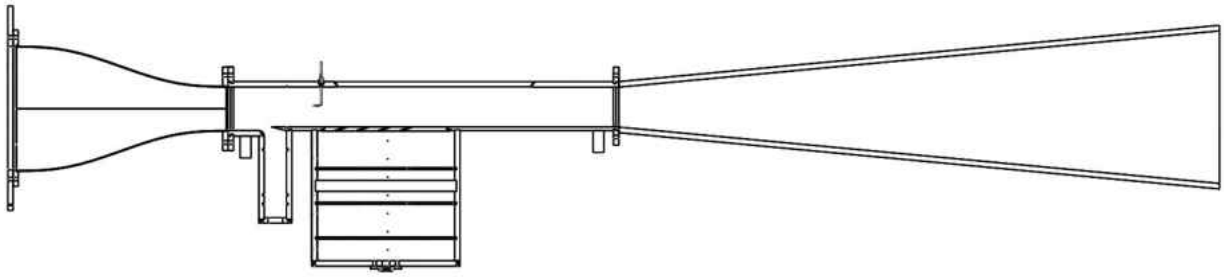

Figure 2.4: Cross section of wind tunnel

The wind tunnel used for this testing is an open loop tunnel, where the primary flow is provided by a 3000 Hz, 15 kW blower, seen in figure 2.4. A Martin JEM ZR44 Hi-mass fog machine was used to seed the primary flow with particles. Directly downstream of the blower is a series

of screens and honey combs to provide flow conditioning. A 6:1 contraction follows the flow conditioning, which reduced the cross sectional area to 5.5" x 11". Upon exiting the contraction, the boundary layer developing from the contraction is then removed by a 2.2 kW boundary layer suction fan. The boundary layer is then re-tripped by means of a sharp edge 3mm in thickness directly downstream of the boundary layer suction, which can also be seen in figure 2.5. This boundary layer trip is located 256mm upstream of the leading edge of the first row of holes. The 'coupons' are manufactured such that the leading edge of the hole breakout is in the same relative location once inserted into the wind tunnel.

The freestream temperature and total pressure are monitored upstream of the first row of holes, by means of a type-T thermocouple and piot tube, respectively. Static pressure measurements are taken at various locations along the side of the wind tunnel. These measurements are used to calculate the freestream density on a per test basis.

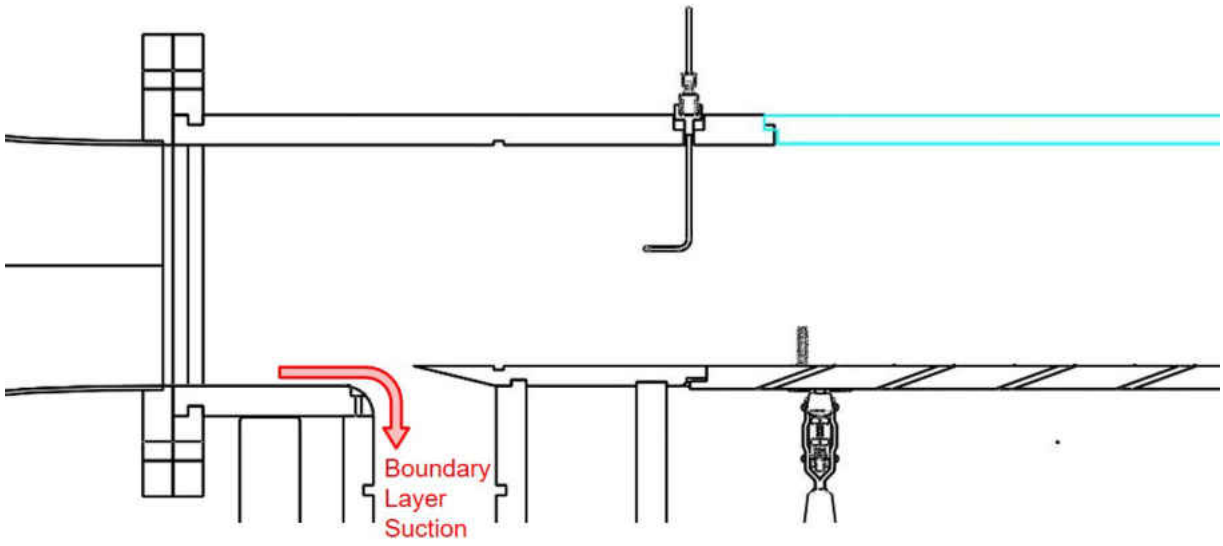

Figure 2.5: Boundary layer suction and trip upstream of test section

2.3 Secondary Flow

The effective density ratios tested in the present study are 1.0 and 1.55, which are achieved by alternating the secondary fluid between Air and CO_2 respectively. Air is supplied by the shop compressor compressor, capable of providing a maximum flowrate of 40 SCFM. Carbon dioxide is supplied as a cryogenic liquid by a MicroBulk CO_2 tank (3500 lb capacity). Immediately downstream of the CO_2 tank, a 30kW electric vaporizer turns the cryogenic liquid into gas and is capable of handling flow rates up to 130 SCFM. The gaseous CO_2 then passes through a passive ambient heat excchanger (located outside of the testing facility) which brings the temperature of the gas close to that of the freestream. The temperature difference between the CO_2 coolant and the freestream is typically no more than 5°C. This temperature difference is typically seen for the low blowing ratios due to the Reynolds number effect in the upstream heat exchanger.

The main supply of coolant is slip into two individual lines, as depicted in figure 2.6. The first of these main lines is routed into a TSI 9307-6 oil droplet generator containing olive oil, with a mean droplet diameter of 1 μm. The olive oil is then bubbled by the incoming air thereby introducing particles into the flow of air. However, the mass flow through the seeder is unable to reach appropriate levels for the desired blowing ratios, while also limiting the ability to vary seeding density. For this reason the second line bypasses the seeder and is then re-coupled with the seeded line, allowing for a greater range of blowing ratios to be reached whilst retaining the ability to control the seeding density.

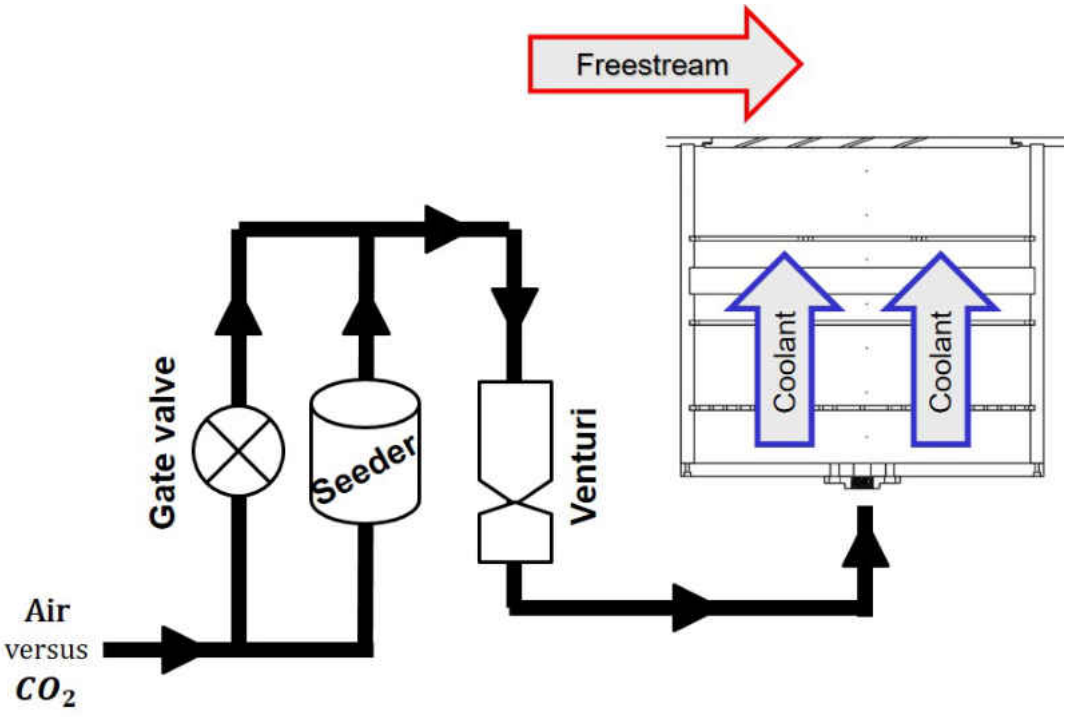

Figure 2.6: Secondary flow piping

Located downstream of the reunion of the two individual coolant lines, the flow passes through a 1”-38 brass venturi. Differential pressure across the venturi, static pressure at the throat, and temperature are all recorded. Once the flow exits the venturi, it is routed into the bottom of the plenum pictured in the top right corner of figure 2.6. Within the plenum, a splash plate followed by a series of screens and honey combs are used to condition the flow. Pressure is recorded at various stages within the plenum to ensure uniformity.

2.4 Particle Image Velocimetry (PIV)

> "Particle image velocimetry, or PIV, refers to a class of methods used in experimental fluid mechanics to determine instantaneous fields of the vector velocity by measuring the displacements of numerous fine particles that accurately follow the motion of the fluid." - Adrian [16]

When introducing particles into a flow, it is crucial to ensure that these particles follow the 'true' path of the fluid. As these particles move throughout the fluid a drag force is imposed by the fluid onto the particles, and is a function of both the fluid and particle. The drag experienced by the particles can be estimated, thus verifying that the particle accurately follows the path of the fluid.

With the use of the TSI 9307-6 oil droplet generator the resulting average droplet size is between 0.5 - 1.0 μm [17].

The Kolmogorov length scale can be estimated using Equation 2.1, where ν is the kinematic viscosity of the fluid and ϵ is the dispersion rate [18].

$$\eta = (\frac{\nu^3}{\epsilon})^{1/4} \tag{2.1}$$

The dispersion rate can be estimated using Equation 2.2, with U being the velocity and L being the characteristic length.

$$\epsilon \sim \frac{U^3}{L} \tag{2.2}$$

With a freestream velocity of 35 m/s and a characteristic length of 6", the estimated dispersion rate would be $\epsilon \sim 281$ kJ/kg/s. The resulting Kolmogorov length scale is then estimated to be η = 10 μm. With the dispersion rate known, the Kolmogorov time scale can then be determined using Equation 2.3.

$$\tau = (\frac{\nu}{\epsilon})^{1/2} \tag{2.3}$$

The estimate for the Kolmogorov time scale is calculated to be τ = 7 μs. Using the Kolmogorov time scale a reasonable estimate for the angular frequency of turbulent motion (ω) can be made [19]. With the angular frequency known, the stokes number can then be calculated using Equation 2.4.

$$S_k = d_p(\frac{\omega}{\nu})^{1/2} \tag{2.4}$$

The resulting Stokes numbers are 0.23 and 0.37 for the injection of air and CO_2, respectively. Samimy [20] showed that a particles response is well characterized by the Stokes number, as the velocity measurement errors grow linearly with Stokes number. As a result, it was determined that a Stokes number of 0.2 produces an error of approximately 2%.

2.4.1 Hardware Setup

The laser used in the present study is an Evergreen Nd:YAG dual pulsed laser manufactured by Quantel. The sheet produced by the laser has a wavelength of 532 nm and a maximum possible power output of 200mJ. Once emitted from the laser head, the beam travels through a pair of biconvex spherical lenses 25.4 mm in diameter with focal lengths of $\pm$ 150mm respectively. These

cylindrical lens are mounted within a transnational tube, allowing the thickness of the laser sheet to be altered by changing the effective focal length. The condensed beam then reflects off a 45°turning mirror and through a plano-concave cylindrical lens that spreads the beam into a sheet. The above described laser setup is mounted overhead of the wind tunnel such that the laser sheet enters the testing area through an acrylic top lid, seen in figure 2.7. A cross-section view of the wind tunnel with the laser sheet super imposed to display the location and orientation relative to the film cooling configuration can be seen in figure 2.8.

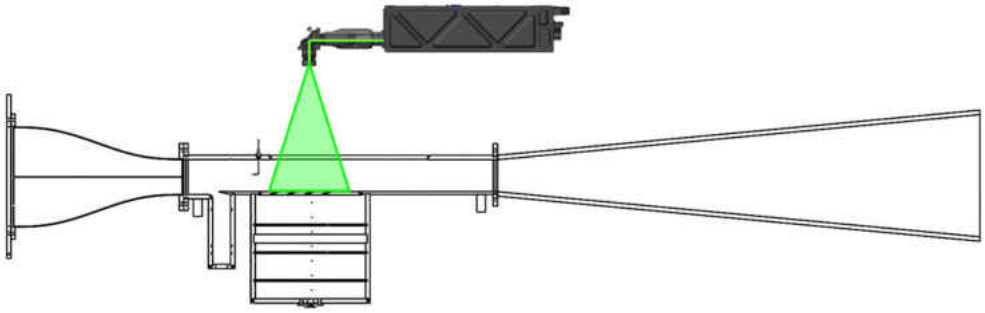

Figure 2.7: Laser head orientation relate to tunnel

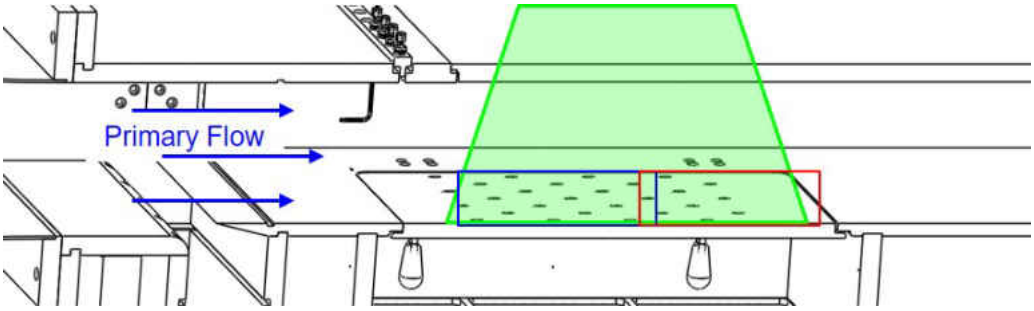

Figure 2.8: Tunnel cross-section showing laser sheet location and orientation

Dotted gird paper with a know grid spacing and dot size is adhered to a flat piece of acrylic that is used as a calibration grid. The calibration grid is used to align both the laser sheet to the testing area during setup and the cameras to ensure that the entire flow field is captured. Additionally, this calibration grid is used during post-processing to convert the images from pixels to millimeters. The calibration grid oriented such that it intersects the centerline of the center-most column of holes.

Two Andor Zyla CMOS 5.5 megapixel cameras are used simultaneously to capture the entire flow field within the testing area. In addition, the approximate locations of the images captured by the first and second camera, represented by the blue and red rectangles, is shown in figure 2.8. Attached to each of the cameras is a 35mm lens with ND2 filter. The timing of the two cameras and the laser are synced via LabVIEW, where the triggering, exposure time, frequency, and time between laser pulses can all be controlled.

The timing between laser pulses directly relates to the overall displacement of a particle captured by the cameras for a given set of images. Nogueira et al. [21] explains that the displacement of a particle should be no larger than one quarter of the intended interrogation window size. Due to the nature of the present experiment, a large range of velocities is anticipated and therefore a time delta must be chosen capable of resolving this range. By using the guidelines outlined by Adrian [16] the determined time delta between laser pulses is 10 μs, yielding particle displacements in the range of 6 to 12 pixels.

2.4.2 Pre-processing

The raw images are exported from the Andor software as a *.tif file. Each of the sets of images are imported on a per camera and per test basis, recall that two cameras are used to capture the flowfield for a single test case. Once all of the images have been imported, a calibration is preformed for

each of the cameras using the calibration images mentioned earlier. This calibration process allows the conversion of the images from pixel space to millimeters. For reference, it was determined that a single pixel within the flowfield is approximately 0.41 mm by 0.41 mm.

With the conversion of the raw images from pixel space to the real world, the images pre-processed to prepare them for vector calculations. Again, the following pre-processing steps are preformed on a per camera and per test basis. The images are grouped into a Mutliframe according to their respective image pair, which in this case is as follows: 1+2, 3+4, 5+6, etc. Once sorted into their respective image pairs, default attributes are then added to the pairs designating the respective calibration to use (dependent on the camera) and the time delta between images in the pair.

In an attempt to reduce the quantity of erroneous vectors as a result of performing Particle Image Velocimetry, the raw images are masked such that only the desired portion of the image undergoes vector calculations. As previously mentioned, reflections are a major concern when preforming PIV and should be mitigated when possible. While the best practices outlined by Adrian [16] were followed resulting in a great reduction in the quantity and severity of the reflections, due to the configuration studied it was not possible to eliminate all reflections. As a result, the masking function was used primarily to exclude the high intensity saturation captured due to these reflection.

2.4.3 Performing PIV

Based on guidelines suggested by Adrian [16] for best practices while preforming PIV, the particle shift should be no less than a 1/4 of the interrogation. In order to accommodate the large range of anticipated velocities decreasing sizes of interrogation windows are used during processing. An initial pass is preformed with a 64 by 64 pixel window to capture the large displacement vectors in the freestream. Then 4 passes are made using a 24 by 24 pixel window with an auto adaptive

window, allowing the shape of the interrogation window to change, making the center more crucial than the edges.

2.4.4 Post-processing

While the presence of erroneous vectors is unavoidable, the percentage of of false vectors can be below 5 $\%$ for carefully configured configurations [21]. In order to remove any spurious vectors, a suitable magnitude range is defined for both the wall normal and streamwise velocity components. These velocities ranges are defined such that all possible/anticipated velocities within the field of view are accepted, while those that fall outside of this range are removed. This processes is done iteratively by incrementally increasing/decreasing the bound of the acceptable velocity magnitudes to ensure that there is no cropping of the data.

Additionally, the mean and standard deviation are calculated for a given interrogation window within the field of view. Once calculated, these statistics are compared to the immediate surrounding interrogation windows. If the statistics do not fall within a defined range of one-another, the next highest correlation peak is examined. In the event that a suitable vector is not found, the resulting vector is then left empty.

CHAPTER 3: RESULTS AND DISCUSSION

Found in this chapter are comparisons of the streamwise velocity contours (section 3.1), tracking jet trajectory (section 3.2), pressure gradient calculations (section 3.3), and downstream momentum thickness (section 3.4). A complete listing of each test case present in this study can be found in table 3.1. Throughout this chapter, the leading and trailing edges of the first, third, fifth, and seventh rows of injection are represented by magenta diamond respectively. Recall, that all data displayed in this chapter are a result of the tests taken down the centerline plane for both the cylindrical and fan-shape configurations.

The contour comparisons are made by independently holding either blowing ratio (M), momentum flux ratio (I), or velocity ratio (V) constant while density ratio (DR) is varied. The above mentioned comparisons are made for both the cylindrical film cooling configuration and the fan-shape film cooling configuration. A complete listing of the cases used in the comparison of blowing ratio, momentum flux ratio, and velocity ratio can be found in tables 3.2, 3.3, and 3.4 respectively. Seen in each of the above mentioned tables are the testing conditions and film cooling configuration used for each of the cases within a comparison.

Jet trajectory results are displayed only for the cylindrical configuration due to limitations in determining the trajectory of the coolant as it moves throughout the boundary layer. These results provide insight into the variation of downstream influence versus blowing ratio and density ratio.

Momentum thickness is calculated at each downstream location for the provided test matrix. By examining the resulting momentum thickness, the resulting influence of the injection on the theoretical wall normal displacements are observed.

Table 3.1: Present study test matrix

Test Number	M	I	V	DR	Configuration
110	0.40	0.15	0.39	1.02	Cyl
111	0.47	0.22	0.46	1.02	Cyl
112	0.52	0.26	0.51	1.03	Cyl
113	0.64	0.40	0.62	1.03	Cyl
114	0.72	0.51	0.70	1.03	Cyl
115	0.80	0.63	0.78	1.03	Cyl
116	1.01	1.00	0.98	1.03	Cyl
117	1.16	1.31	1.12	1.04	Cyl
118	1.45	2.02	1.39	1.04	Cyl
119	0.32	0.07	0.21	1.54	Cyl
120	0.51	0.17	0.33	1.55	Cyl
121	0.56	0.20	0.36	1.55	Cyl
122	0.74	0.36	0.48	1.55	Cyl
123	0.81	0.42	0.52	1.56	Cyl
124	1.02	0.66	0.65	1.57	Cyl
125	1.23	0.95	0.78	1.58	Cyl
126	1.34	1.13	0.84	1.58	Cyl
130	0.52	0.27	0.51	1.02	Diff
131	0.64	0.40	0.63	1.02	Diff
132	0.72	0.50	0.70	1.02	Diff
133	0.85	0.71	0.83	1.02	Diff
134	1.04	1.04	1.01	1.03	Diff
135	1.18	1.35	1.15	1.03	Diff
138	0.50	0.16	0.33	1.55	Diff
139	0.69	0.31	0.45	1.55	Diff
140	0.80	0.41	0.52	1.55	Diff
141	1.01	0.65	0.64	1.57	Diff
142	1.16	0.85	0.73	1.58	Diff

3.1 Streamwise Velocity Contour Comparison

3.1.1 Constant Blowing Ratio

Contour plots presented in this section are grouped based on the ratio and configuration used for the comparison. Within each of the presented figures, each case is individually labeled with the case specific ratio value, density ratio, film cooling configuration, and test number.

Streamwise velocity contours are shown for each of the comparisons listed in tables 3.2, 3.3, and 3.4 in figures 3.1 through 3.22. These figures give an idea of the flowfield produced by the introduction of coolant into the boundary layer through both the cylindrical and fan-shape configuration.

Table 3.2: Constant blowing ratio comparisons

Comparison Number	M	DR	Configuration	Test Number
M1	0.40	1.02	Cyl	110
	0.32	1.54	Cyl	119
M2	0.52	1.02	Cyl	112
	0.51	1.55	Cyl	120
	0.52	1.02	Diff	130
	0.50	1.55	Diff	138
M3	0.72	1.03	Cyl	114
	0.74	1.55	Cyl	122
	0.72	1.02	Diff	132
	0.69	1.55	Diff	139
M4	1.01	1.03	Cyl	116
	1.02	1.57	Cyl	124
	1.04	1.03	Diff	134
	1.01	1.57	Diff	141
M5	1.16	1.04	Cyl	117
	1.23	1.57	Cyl	125
	1.18	1.03	Diff	135
	1.16	1.58	Diff	142

Comparisons between low and high density ratio injections discussed in this section are done at nominal blowing ratio values of M = 0.35, 0.5, 0.7, 1.0, and 1.2 Comparisons between film cooling configuration can also be seen within these comparison, except at blowing ratios M = 0.35 and 1.4. A complete listing of the cases used within each blowing ratio comparison can be found in table 3.1.

The lowest blowing ratio comparison of M = 0.4 for the lower density fluid and M = 0.32 for the higher density fluid for the simple cylindrical configuration is shown in figure 3.1. In both cases, the jets can be seen staying attached to the wall throughout the entire film cooling array. As the flow moves downstream, the boundary layer is seen to thicken with each row of injection. In the near wall region low velocity coolant can be seen just downstream of the first jet. This low velocity fluid can be seen to extend further in the wall normal direction with each row of injection.

The blowing comparison of M = 0.5 for the cylindrical film cooling configurations, for the low density ratio DR = 1.02 and high density ratio DR = 1.55 are displayed in figure 3.2. The low density injection for the cylindrical configuration begins to show more of a presence off the wall than seen for the previous comparison M1. When comparing the high and low density injections for the simple cylindrical configuration, the higher density fluid can be seen to have consistently larger downstream regions of low velocity. This is due to the lower density region injecting with a greater velocity than that of the higher density.

The fan-shape configuration comparison with blowing ratios of M = 0.52 and M = 0.5 for the low and high density ratios, respectively, is seen in figure 3.3. Similar to what was seen for the simple cylindrical configuration at this blowing ratio, the higher density fluid for the fan-shaped injection is seen to have a more pronounced low velocity region in the near wall region than that of the low density case.

When comparing the two configurations tested, the fan-shaped configuration can be seen

to have a more uniform low velocity region developing in the near wall region to that of the cylindrical cases. Specifically, seen just downstream of the fifth row of holes for the high density cylindrical case is a small, local region of slightly elevated velocity that can be associated with the coolant produced by the injection, seen in figure 3.2. This high velocity region doesn't present its self in the fan-shape configuration, and is a result of the decreased velocity due to the expanded hole area prior to injection.

Comparison M3 shows is the first indication of the jets lifting off the surface. The low velocity fluid in the near wall region has diminished dramatically for the low density injection from the cylindrical configuration, seen in figure 3.4. The boundary layer is seen to thicken with each row of injection, thereby allowing the following (downstream) row of holes to penetrate deeper into the boundary layer. A high velocity core located directly downstream of injection can be seen penetrating in to the boundary layer for this low density, cylindrical case. An increase in coolant penetration can also be seen for the high density cylindrical configuration. However the high density cylindrical injection retains, to some degree, the downstream low velocity regions, suggesting that the coolant maintains its surface attachment more so than the lower density injection.

Unlike the cylindrical configuration, the fan-shape injection continue to show a low velocity region in the near wall region, seen in figure 3.5 Again, this due to the expanded exits of the fan-shape configuration, allowing the velocity to decrease prior to injection This suggests that the coolant is remaining close to the wall, and as expected offering improved performance over the cylindrical configuration.

Comparison of blowing ratio M = 1 for high and low density injection for the cylindrical configuration is shown in figure 3.6. When observing the cylindrical cases for both density injections, jet detachment from the surface is clear present. A low velocity region is seen upstream of the injection from a row of holes. This is associated with the blockage in the flow produced as the

high velocity jet exits the film cooling hole. Seen specifically in the lower density injection of the cylindrical configuration, the high velocity core produced per jet maintains an elevated magnitude for a larger downstream distance with each row of injection. These high velocity cores can also be seen in the higher density cylindrical injection case.

The fan-shape configuration continues maintain low velocity fluid in the near wall region, seen in figure 3.7. Again the higher density injection is observed to sustain an thicker layer of low velocity fluid in the near wall region per streamwise location than that of the lower density fluid. The presence of the jet beginning to lift off the surface is seen downstream of the third row of injection at x/d = 15.7 for the high density injection of the fan-shape configuration. When compared to the blowing ratio M = 0.72, the low density injection of the fan-shape configuration seen at M = 1 appears to have a thinning layer of low velocity fluid in the near wall region.

The constant blowing ratio comparison of M = 1.2 for the cylindrical and fan-shaped configurations, can be seen in figure 3.8 and figure 3.9 respectively. Similarities are seen between the low and high density ratios for the cylindrical film cooling configuration for this comparison. The high velocity core produced by the jet detaching from the surface is comparable is size and wall normal elevation between both density ratios. The low velocity region upstream of the fifth row of injection is larger for the higher density fluid than the lower density case. Continued thinning of the low velocity layer seen in the near wall region is observed for both density ratios injected through the fan-shaped film cooling configuration. The high density case for the fan-shaped configuration has significantly more low velocity coolant present in the near wall region than that of the lower density. This suggests that the higher density coolant is remaining closer to the surface, offering improved coverage over the lower density injection. However, faint suggestions of the beginning of jet detachment from the surface are evident for the higher density ratio, as seen at x/d = 15.7.

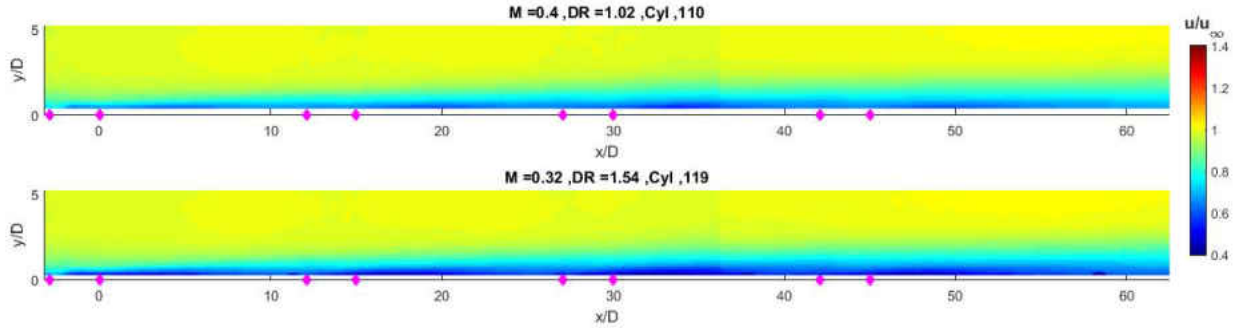

Figure 3.1: u contour of cylindrical M1

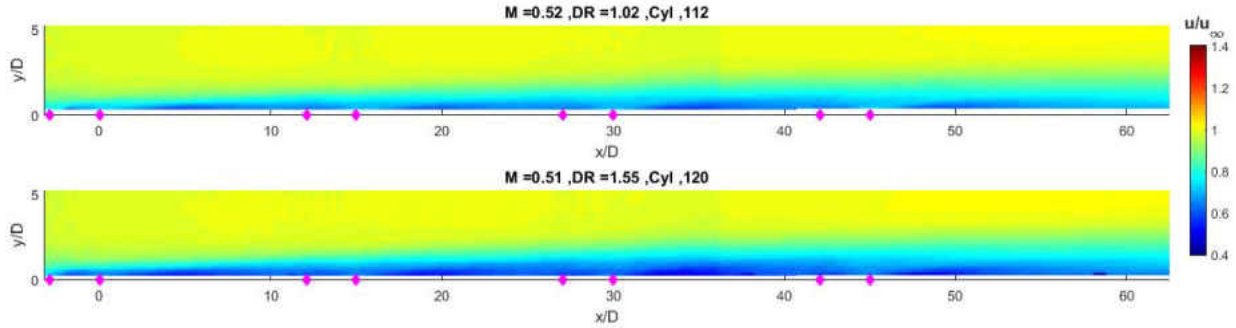

Figure 3.2: u contour of cylindrical M2

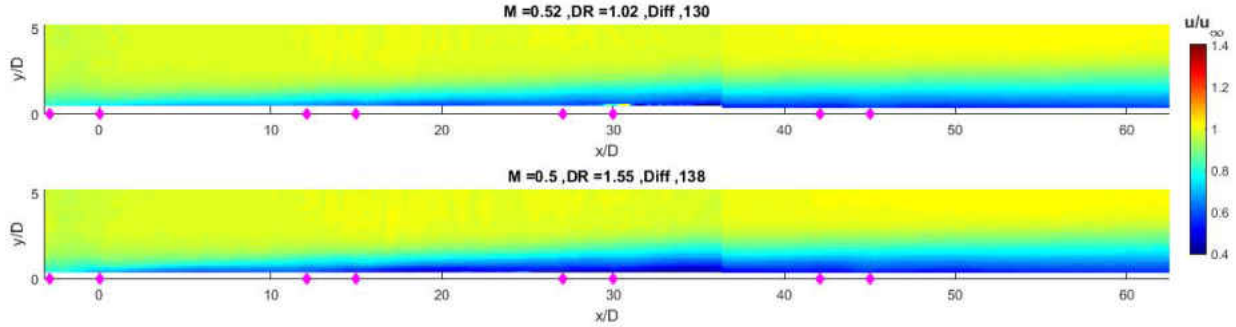

Figure 3.3: u contour of fan-shape M2

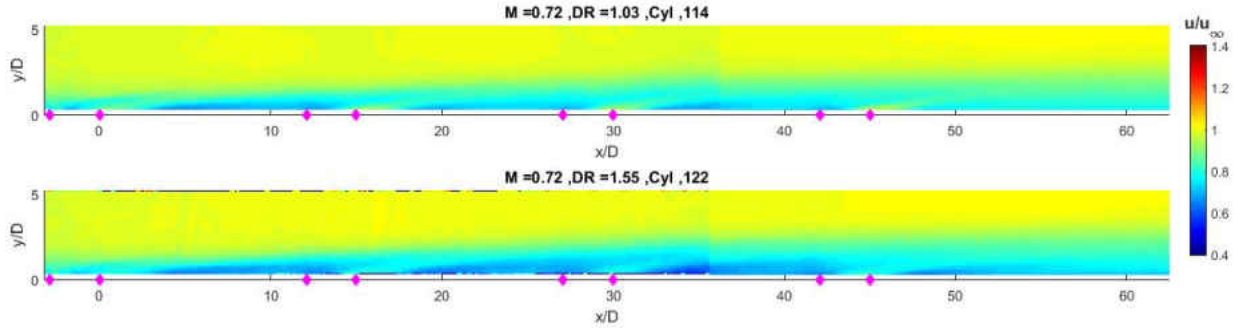

Figure 3.4: u contour of cylindrical M3

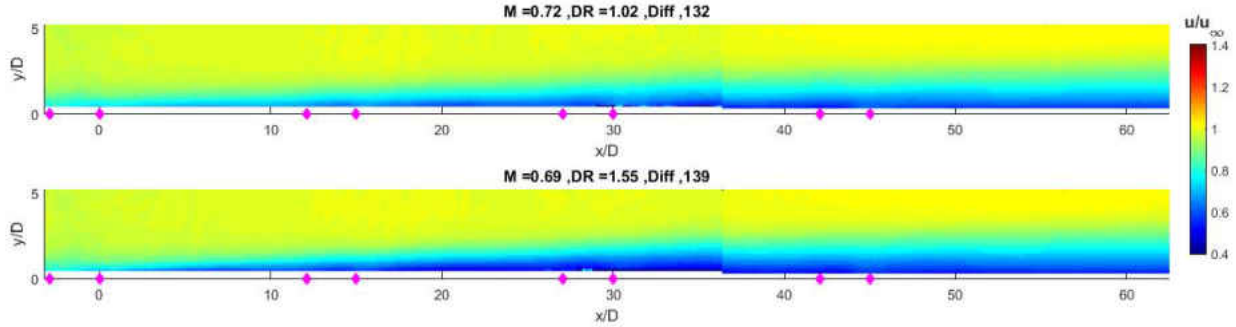

Figure 3.5: u contour of fan-shape M3

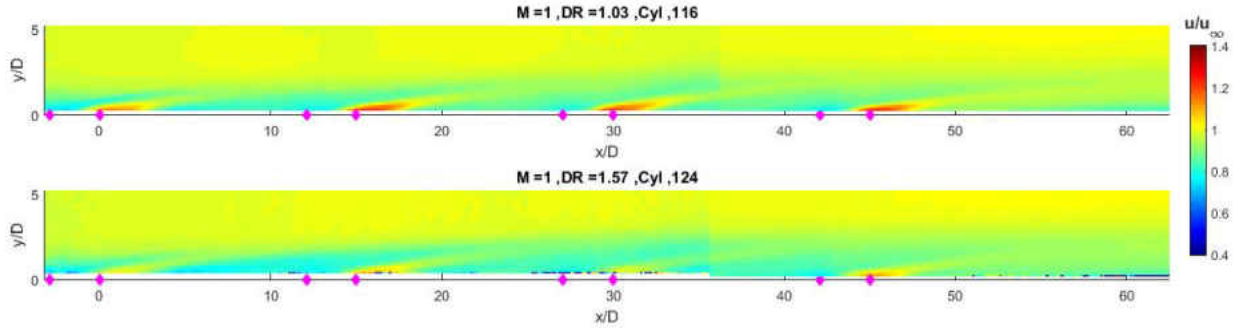

Figure 3.6: u contour of cylindrical M4

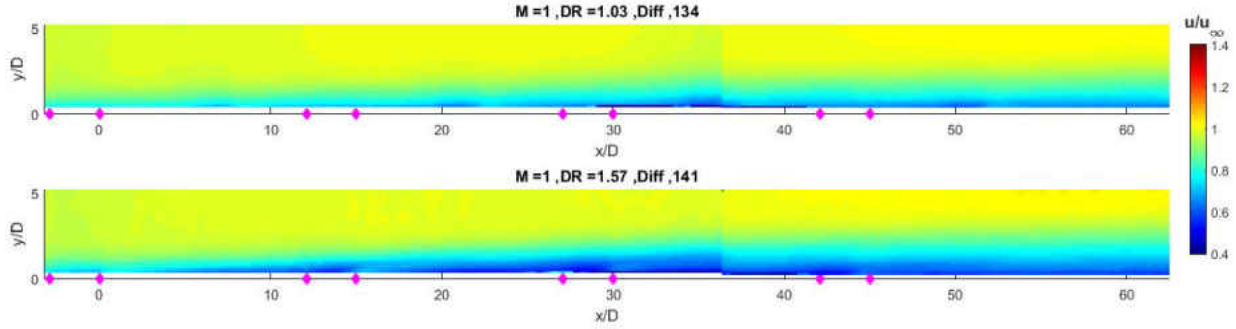

Figure 3.7: u contour of fan-shape M4

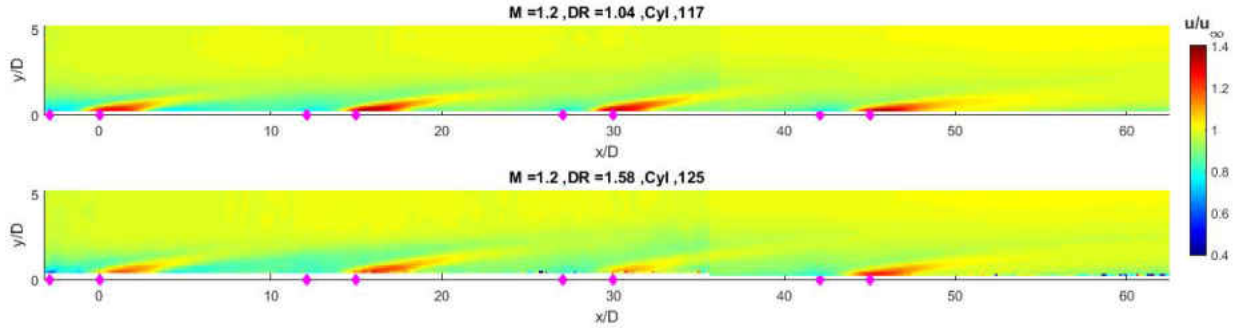

Figure 3.8: u contour of cylindrical M5

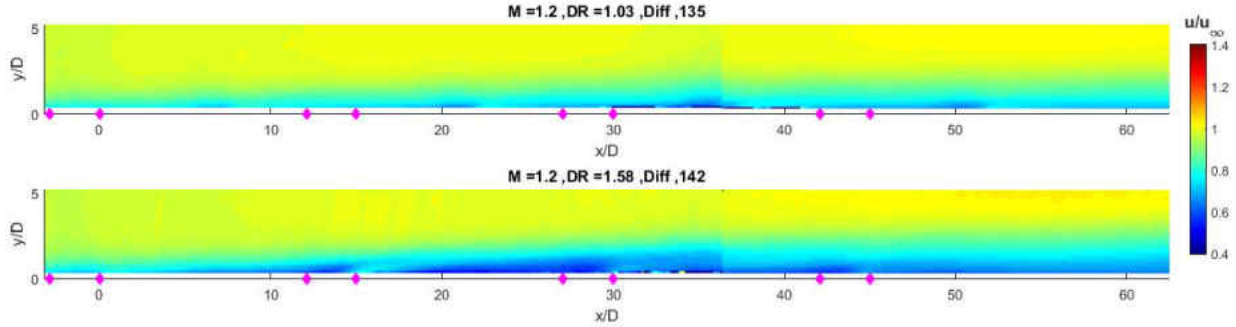

Figure 3.9: u contour of fan-shape M5

3.1.2 Constant Momentum Flux Ratio

Table 3.3: Constant momentum flux ratio comparisons

Comparison Number	I	DR	Configuration	Test Number
I1	0.22	1.02	Cyl	111
	0.20	1.55	Cyl	121
I2	0.40	1.03	Cyl	113
	0.42	1.56	Cyl	123
	0.40	1.02	Diff	131
	0.41	1.55	Diff	140
I3	0.63	1.03	Cyl	115
	0.66	1.57	Cyl	124
	0.71	1.02	Diff	133
	0.65	1.57	Diff	141
I4	1.00	1.03	Cyl	116
	0.95	1.58	Cyl	125

The lowest constant momentum flux comparison of I = 0.2 for the cylindrical configuration can be seen in figure 3.10. The higher density fluid presents a thicker layer of lower velocity fluid in the near wall region that that of the lower density injection. This can be associated with the increased mass injected for the elevated density ratio required to match the momentum flux ratio of the lower density fluid. Additionally, the increased thickness of the boundary layer for the high density injection can also be attributed to the increased mass introduced by this higher density fluid.

The momentum flux ratio comparison of I = 0.4 can be seen for the cylindrical and fan-shape configurations in in figure 3.11 and figure 3.12, respectively. For the cylindrical configuration, the higher density injection shows reduced amounts of low velocity in the near wall downstream mixing regions when compared to that of the lower density ratio. Also, the boundary layer downstream of the seventh row of injection is thicker for the higher density ratio injection. Again, this can be explained by the elevated blowing ratio required by the higher density fluid

when matching the momentum flux ratio with that of the lower density ratio. However, the high density injection for the fan-shape configuration retains a thicker layer of low velocity fluid in the near wall region over that observed for the lower density fluid.

The constant momentum flux ratio comparison of I = 0.65 for the cylindrical configuration can be seen in figure 3.13. The higher density ratio case can be seen to have a larger region of elevated streamwise velocity immediately downstream of the holes and penetrates further into the boundary layer that its lower density ratio counterpart. This increased penetration into the boundary is associate with the elevated blowing ratio necessary for the high density ratio to match the momentum of the lower blowing ratio. The fan-shape configuration for the momentum flux ratio comparison of I = 0.65 can be seen in figure 3.14. With the increase of momentum flux ratio from I = 0.4 in the previous comparison to I = 0.65 presented in this comparison, the thickness of the low velocity region in the near wall decreases for both density ratios.

The highest momentum flux ratio comparison for the cylindrical configuration can be found in fgure 3.15. Evidence of jet detachment from the surface is present for both density ratios. The higher density ratio maintains elevated levels of streamwise velocity to further downstream distances upon injection that its lower density ratio counterpart. Additionally, this higher density injection penetrates further into the boundary layer per row.

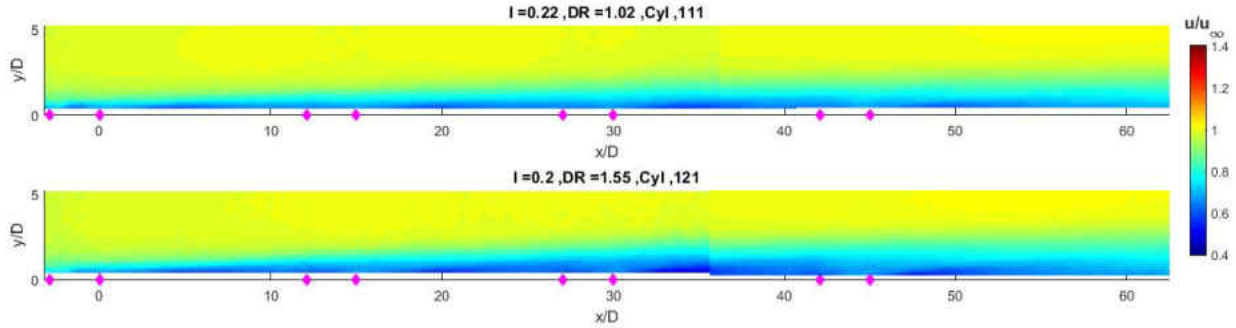

Figure 3.10: u contour of cylindrical I1

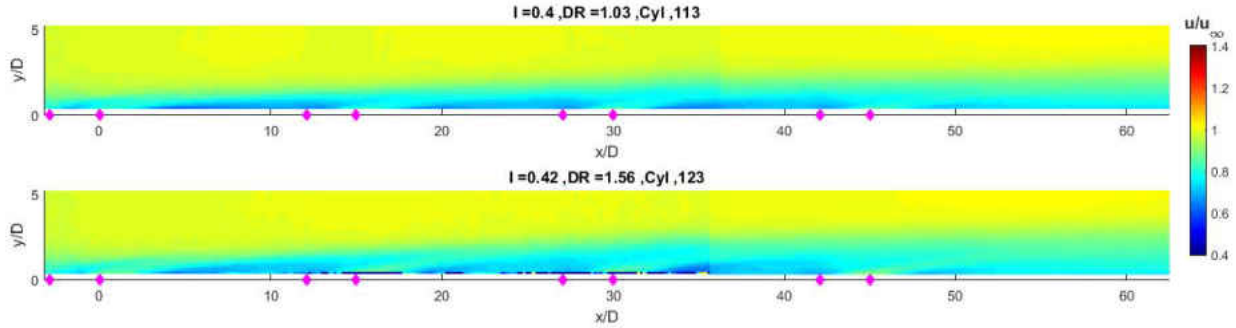

Figure 3.11: u contour of cylindrical I2

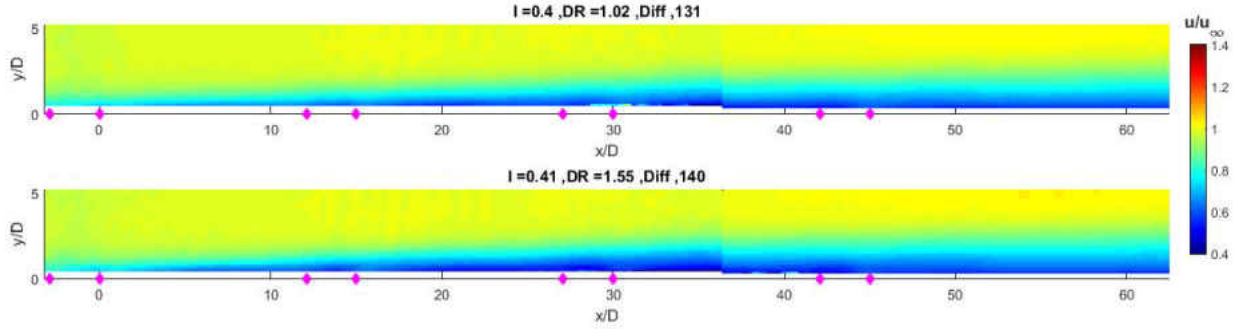

Figure 3.12: u contour of fan-shape I2

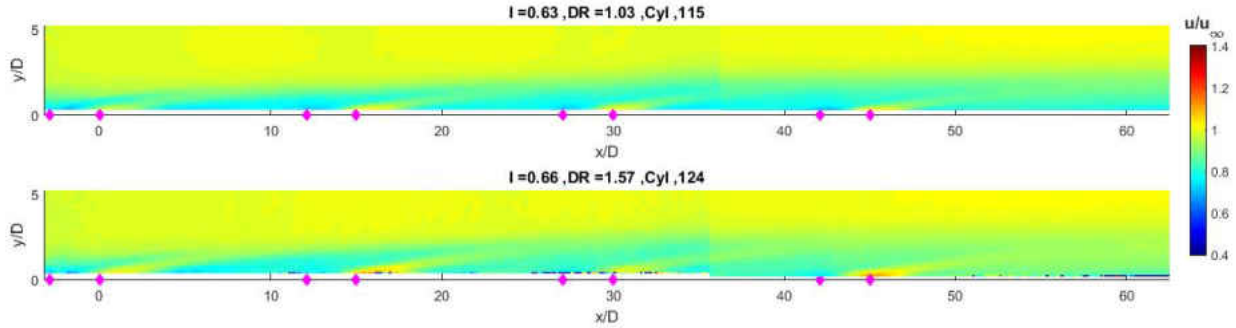

Figure 3.13: u contour of cylindrical I3

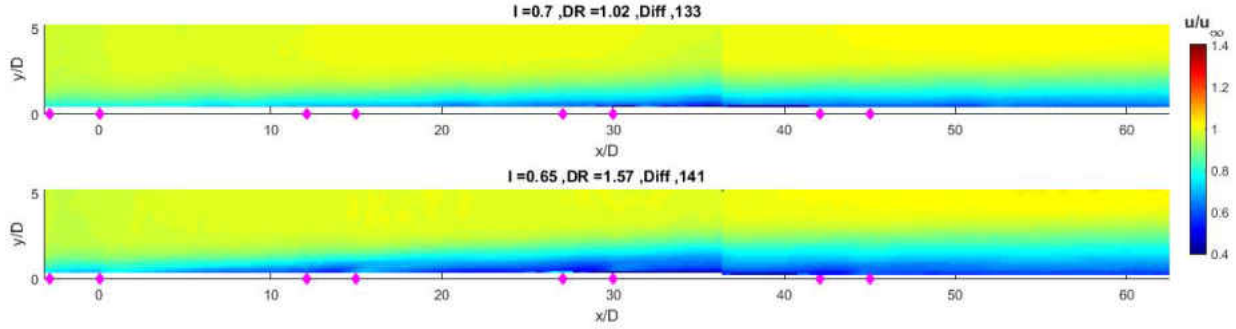

Figure 3.14: u contour of fan-shape I3

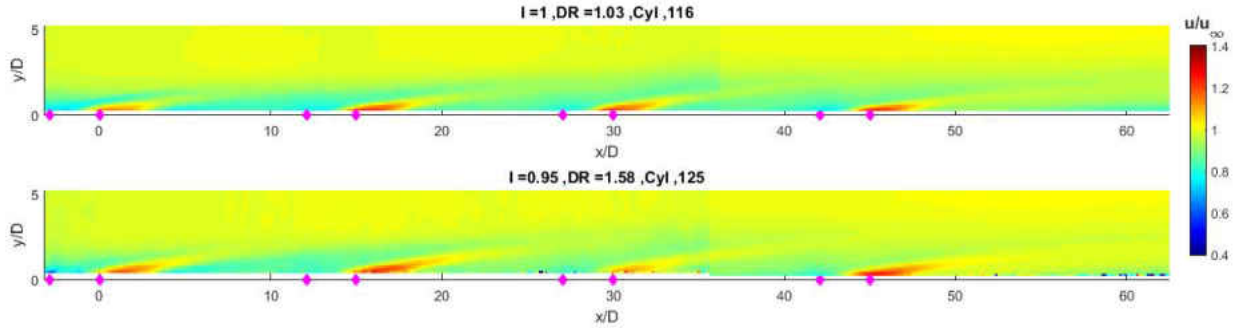

Figure 3.15: u contour of cylindrical I4

3.1.3 Constant Velocity Ratio Comparisons

Table 3.4: Constant velocity ratio comparisons

Comparison Number	V	DR	Configuration	Test Number
V1	0.39	1.02	Cyl	110
	0.36	1.55	Cyl	121
V2	0.51	1.02	Cyl	112
	0.52	1.56	Cyl	123
	0.51	1.02	Diff	130
	0.52	1.55	Diff	140
V3	0.62	1.03	Cyl	113
	0.65	1.57	Cyl	124
	0.63	1.02	Diff	131
	0.64	1.57	Diff	141
V4	0.78	1.03	Cyl	115
	0.78	1.58	Cyl	125
	0.70	1.02	Diff	132
	0.73	1.58	Diff	142

The lowest velocity ratio comparison through the cylindrical configuration of V = 0.39 for the low density ratio and V = 0.36 for the high density ratio can be seen in figure 3.16. The injection of the higher density fluid can be seen to have a large layer of low velocity fluid in the near wall region when compared to that of the low density fluid. Additionally, the higher density ratio injection begins to display the onset on jet detachment with the elevation of streamwise velocity immediately downstream of injection. This elevated velocity downstream of injection in the near wall region can be seen specifically at x/D = 31, and x/D = 45.

The constant velocity ratio comparison of V = 0.5 for the cylindrical configuration can be seen in figure 3.17. Contrary to the previous velocity ratio comparison, the higher density ratio has significantly reduced amounts of low velocity fluid in the near wall region when compared to the low density injection. With the increase in velocity ratio, the higher density ratio injection continues to show increases in surface detachment.

The comparison of low and high density ratio for the constant velocity ratio of V = 0.5 for the fan-shape configuration can be seen in figure 3.18. When compared to that of the cylindrical configuration, the diffuser shaped hole can be seen to retain an elevated thickness of low velocity fluid in the near wall region. This is again to due the decrease in velocity upon injection of the coolant into the boundary layer by the lateral expansion of the hole. The higher density injection shows a thicker layer of the low velocity fluid over that of the low density injection, suggesting that the higher density fluid offers improved coverage at this velocity ratio.

With the velocity ratio increased to V = 0.6, the injection of the higher density fluid can be seen to detach entirely from the surface in figure 3.19. Comparatively, the injection of air at a similar velocity ratio is observed to retain pockets of low velocity fluid in the near wall region. However, with the increase in velocity ratio the injection of the lower density fluid begins to show elevated streamwise velocities downstream of injection, suggesting the onset of jet liftoff.

The constant velocity ratio comparison of V = 0.6 for the fan-shape configuration can be seen in figure 3.20. When compared to the injection through the cylindrical configuration at a similar velocity ratio, the fan-shape holes can again be seen to have increased amounts of low velocity fluid in the near wall region. The higher density fluid is observed to produce a thicker layer of low velocity coolant in the near wall region than that of the low density fluid. Observed downstream of the third row of injection for the higher density fluid, at approximately x/D = 16, is a local high velocity region. As seen previously in the cylindrical configuration, this local high velocity region directly downstream of injection suggests that the coolant is nearing surface detachment.

An increased constant velocity ratio comparison of V = 0.78 for the cylindrical configuration can be seen in figure 3.21. Immediately noticeable for both the low and high density ratio injections in the presence of jet detachment. However, the severity of the liftoff vastly differs be-

tween the two density ratios. The higher density fluid can be seen to have a great core velocity upon immediate injection into the boundary layer, and have a great downstream influence than that of the lower density injection. Additionally, the length of the downstream influence for the higher density ratio can be seen to increase with each row of injection.

By increasing the velocity ratio to that of V = 0.7, the higher density injection through the fan-shape configuration continues to show an increase in the onset of jet detachment, as seen in figure 3.22. Immediately downstream of the third row of injection, at approximately x/D = 16, the magnitude and presence of the high velocity region have increased. Additionally, the low velocity region downstream of the seventh row of injection is observed to decrease in thickness with the increase in velocity ratio.

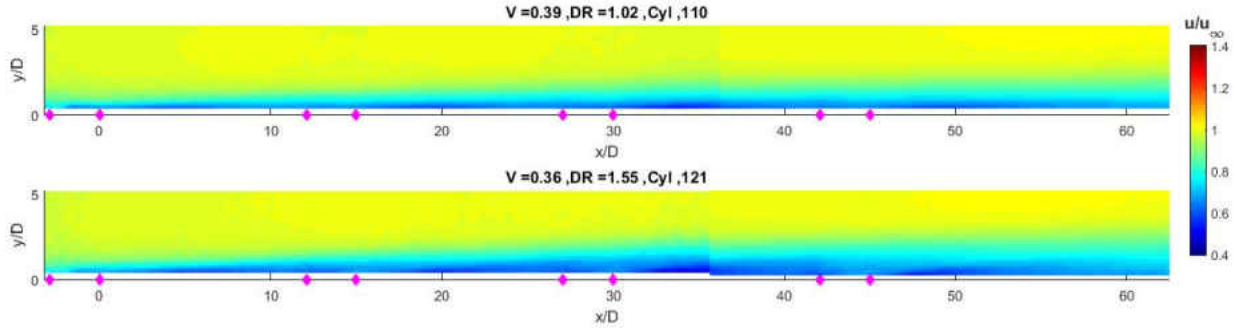

Figure 3.16: u contour of cylindrical V1

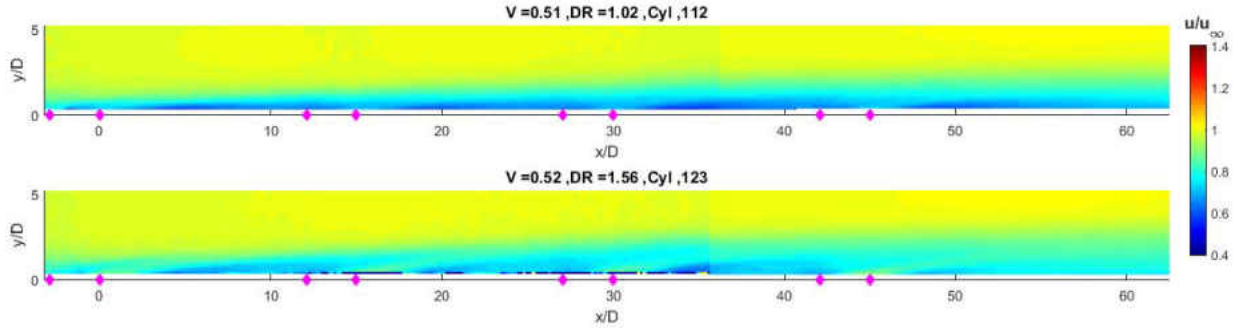

Figure 3.17: u contour of cylindrical V2

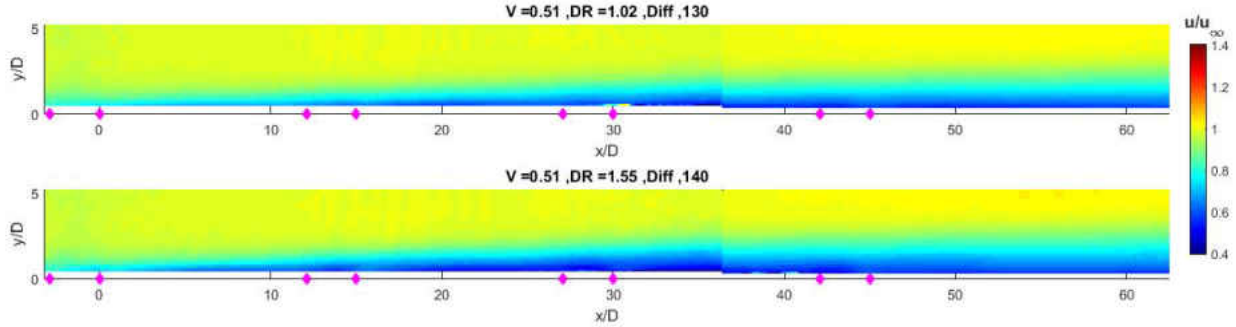

Figure 3.18: u contour of fan-shape V2

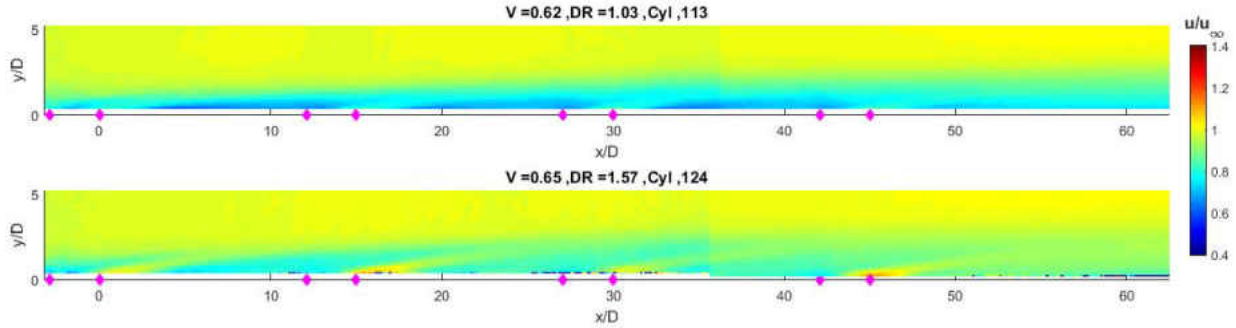

Figure 3.19: u contour of cylindrical V3

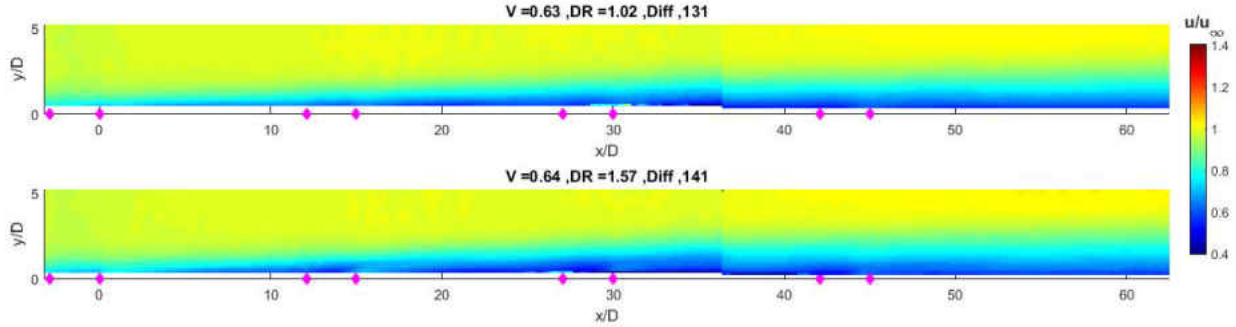

Figure 3.20: u contour of fan-shape V3

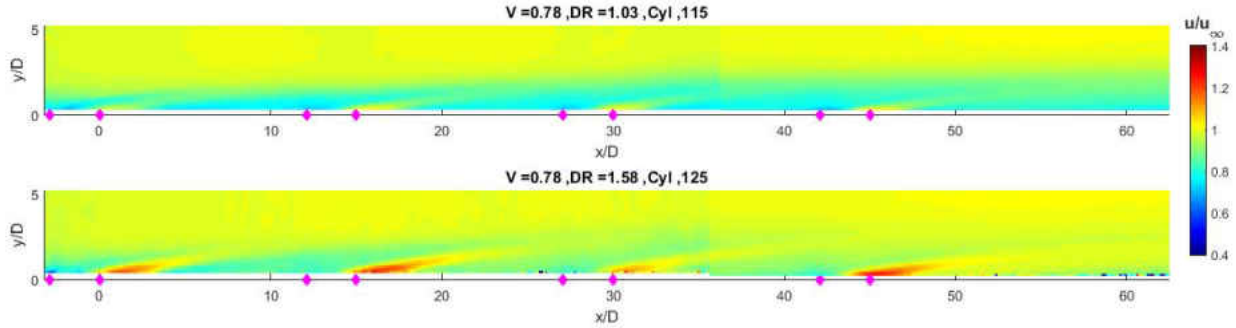

Figure 3.21: u contour of cylindrical V4

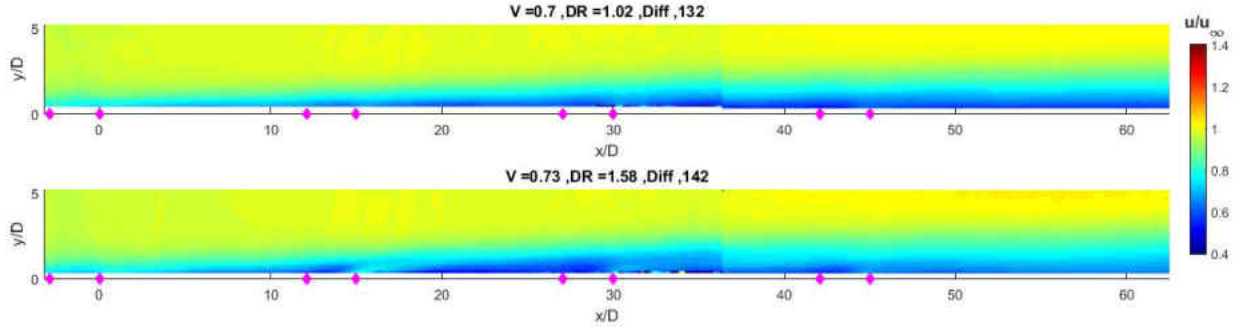

Figure 3.22: u contour of fan-shape V4

3.2 Jet Trajectory Tracking

When studying the effects of various ratios on the jet structure emanating from a film cooling geometry, the ability to classify the trajectory and downstream distance of penetration into the boundary layer provides great insight into the performance for a specific configuration. The ability to classify the trajectory of the jet can be somewhat controversial as there can be several different methods used to determine the path the jet travels. For the present study, the trajectory of the jet was determined by tracking the maximum peak in the streamwise velocity per downstream location which is taken to be the center of the jet as it penetrates into the boundary layer, as seen in figure 3.23. Additionally, the deficit in the velocity profile located above the maximum is also tracked and used as a reference for the overall half width of the jet as it interacts with the boundary layer, seen in figure 3.24. Figure 3.25 shows the streamwise velocity contour where the velocity profiles seen in figure 3.23 and figure 3.24 are taken at the downstream location represented by the solid black line.

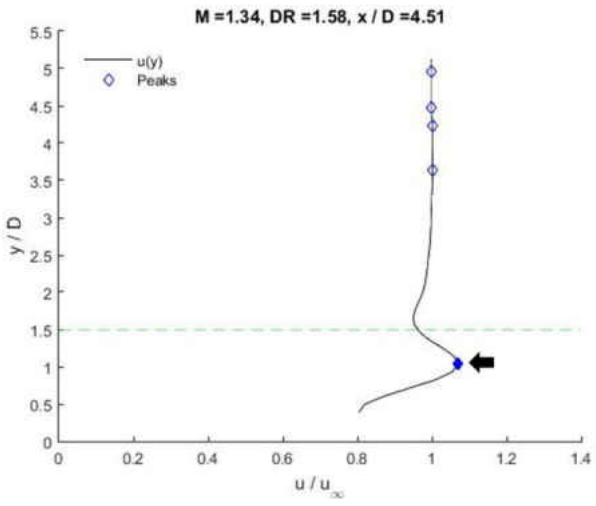

Figure 3.23: Trajectory tracking: Jet centerline

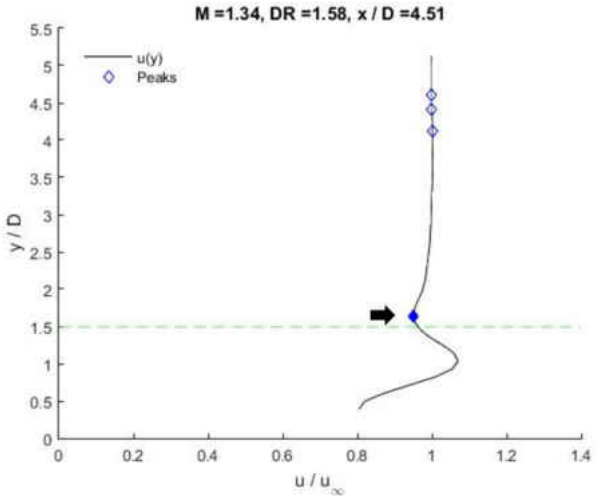

Figure 3.24: Trajectory tracking: Jet edge

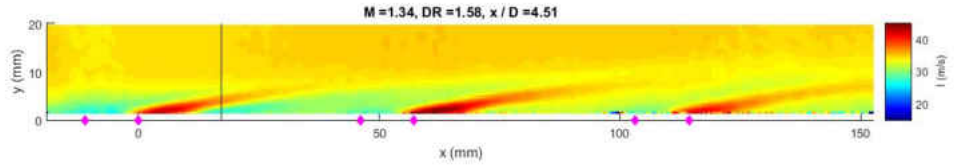

Figure 3.25: Trajectory tracking: Streamwise velocity contour

Since tracking the jet trajectory is solely dependent on the peak in the streamwise velocity profile, the availability of jet trajectory data is limited to the higher blowing ratios where a distinguishing peak can be found. Additionally, due to the increased lateral spreading of the coolant associated with the fan-shaped configuration prior to injection, the natural tendency for the jet to lift off the surface occurs at a much higher blowing ratio than that of the cylindrical

configuration.

Tracking the centerline and upper-bound peaks is preformed on a per downstream location basis, where the resolution of the number of downstream locations is dictated by the number of pixels available for searching. For reference, figure 3.25 is 419 pixels in width by 45 pixels in height, where a pixel is 0.41 mm x 0.41 mm.

The limited resolution of the image presents an issue when attempting to track the centerline and upper-bound of the jet. With the limited resolution, the wall normal height of the peak in the velocity profile is locked to the resolution of the image. To avoid this issue, each column of pixels (representing a discrete downstream location) is curve fit using a cubic interpolator and is then evaluated with a resolution of 0.01 mm. A comparison of the results obtained with and without the use of curve fitting can be seen in figure 3.26. The results from searching for the trajectory of the jet emanating from the first row of holes at a blowing ratio M = 1.34 and a density ratio of DR = 1.58 are shown in figure 3.26.

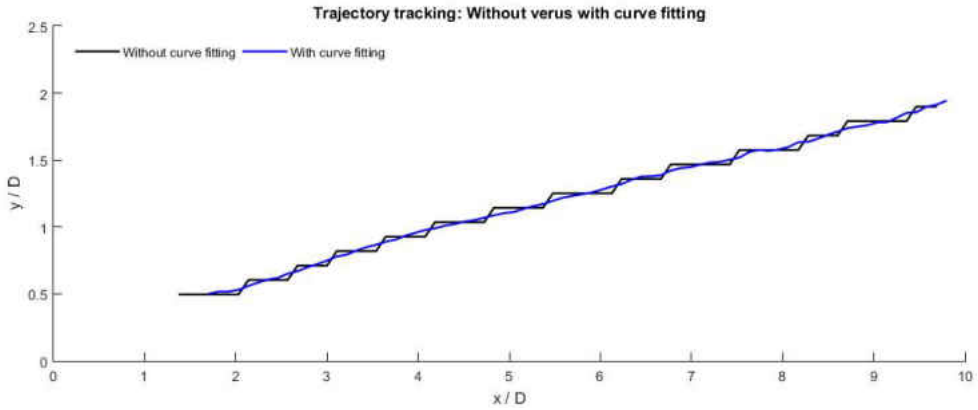

Figure 3.26: Trajectory tracking: Without versus with curve fitting

The trajectory is tracked twice for each row of injection, first for the centerline point then

for the upper bound point, seen in figure 3.23 and figure 3.24. The initial downstream location used to begin searching for the maximum peak in velocity profile (for both the center and upper point) is set at the downstream edge of the row to which the jet is issuing. At the beginning downstream location, the wall normal location of the evaluated peaks are observed. Upon observing the evaluated peaks of the velocity profile, a wall normal limit is defined such that the first peak must be beneath the given wall normal height in order to begin the tracking. This wall normal distance is defined as 1.5D, and is represented as the dashed green line in figure 3.23 and figure 3.24. If this criteria is not met, the search continues to the next available downstream location.

Once the criteria has been met, this downstream location is then checked ensure that the peak that has been picked up is in fact the correct starting location and not a false start. The starting point is checked for being a false start by referencing a defined number of downstream locations to ensure that there exists a peak within a given upper and lower bound of the previous location. Once the first point has been found, the following 5 downstream locations were searched. By defining an allowable range for the following downstream location's peak to be within eliminated the possibility of tracking an incorrect peak. The upper and lower bound of the allowable range to which a peak must reside was defined as $\sigma_{1,2} = 0.25mm$. For reference, the wall normal distance between two downstream locations is approximately 0.05 mm (or roughly 1% of the hole diameter) in figure 3.26.

3.2.1 Trajectory Results

Using the searching procedure outlined in the previous section, the resulting centerline and upper bound trajectories of the jet issuing from a row of holes is determined. The results of the trajectory tracking for the blowing ratio M = 1.34 with a density ratio of DR = 1.58 overlaid on the streamwise velocity contour are shown in figure 3.27. Within the figure, the trajectory for each row of injection

is displayed in a different color, where the solid line represents the centerline trajectory while the dashed line represents the upper limit of the jet.

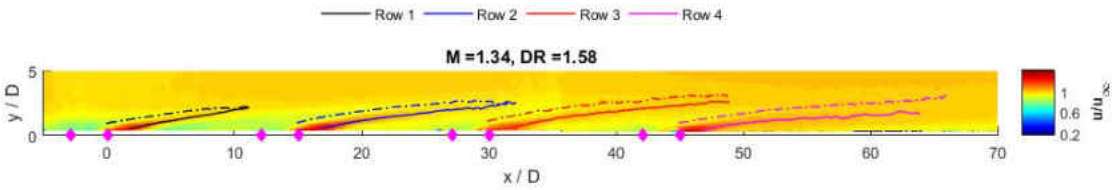

Figure 3.27: Example of trajectory tracking result overlaid on streamwise velocity contour

The effect of blowing ratio on the trajectory and downstream distance of influence per row of injection for the injection of Air and CO_2 can be seen in figure 3.28 and figure 3.29 respectively. Within each of these figures, each row of injection is shown independently containing each blowing ratio. Each color within these figures represents an individual blowing ratio. The solid line for each color represents the centerline trajectory, while the dashed line represents the upper bound, as described in the previous section.

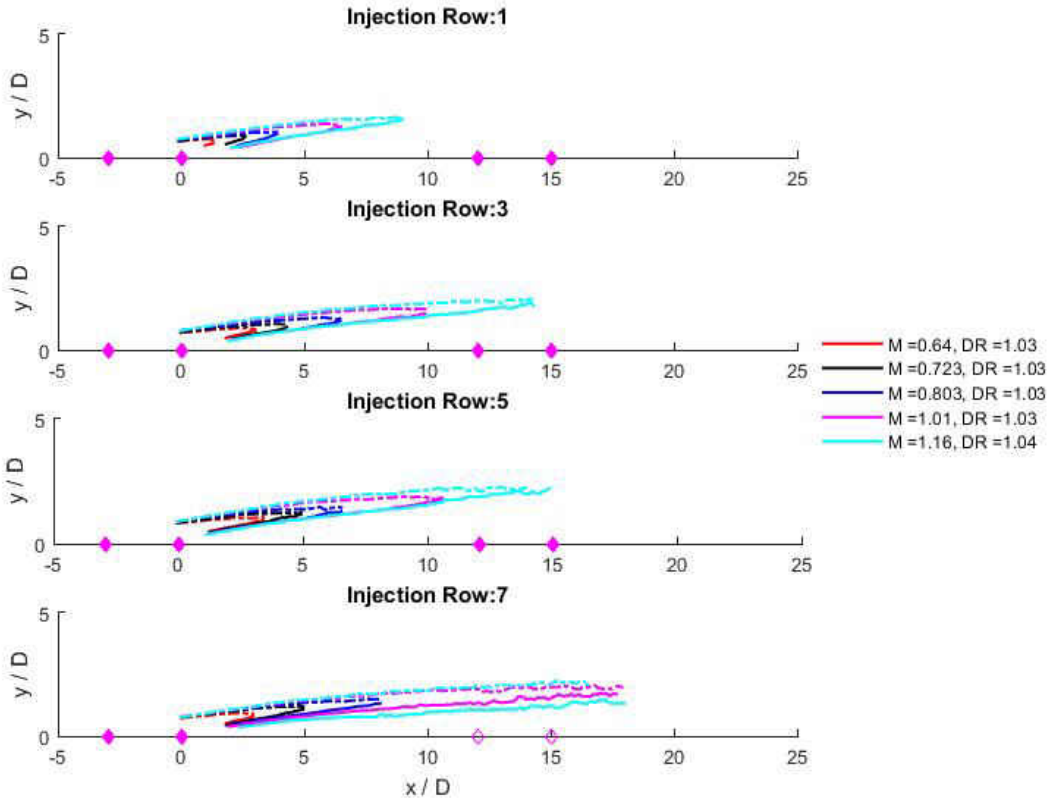

Figure 3.28: Jet trajectory per row of injection per blowing ratio for Air

As expected, the downstream distance of jet penetration increases as blowing ratio increases for all downstream locations, for the injection of both Air and CO_2. When comparing the downstream distance of influence for each of the blowing ratios per row of injection, it is observed that the first row of injection has the shortest overall interaction length. However, the third and fifth rows of injection have a roughly constant total length of interaction for the observed blowing ratios. In comparison, the injection from the seventh row has the greatest downstream interaction

length for all blowing ratios expect for the lowest displayed cases for both Air and CO_2.

When observing the interaction between the jet and boundary layer, a convergence between the centerline trajectory and upper bound is observed for the first, third, and fifth rows, shown in figure 3.28 and figure 3.29. With the exception of the first row, the convergence between the centerline trajectory and upper bound occurs above the preceding row of injection. Specifically, this is seen for the Air blowing ratios of 1.01 and 1.16 in figure 3.28, and the CO_2 blowing ratios of 1.02 and 1.23 in figure 3.29.

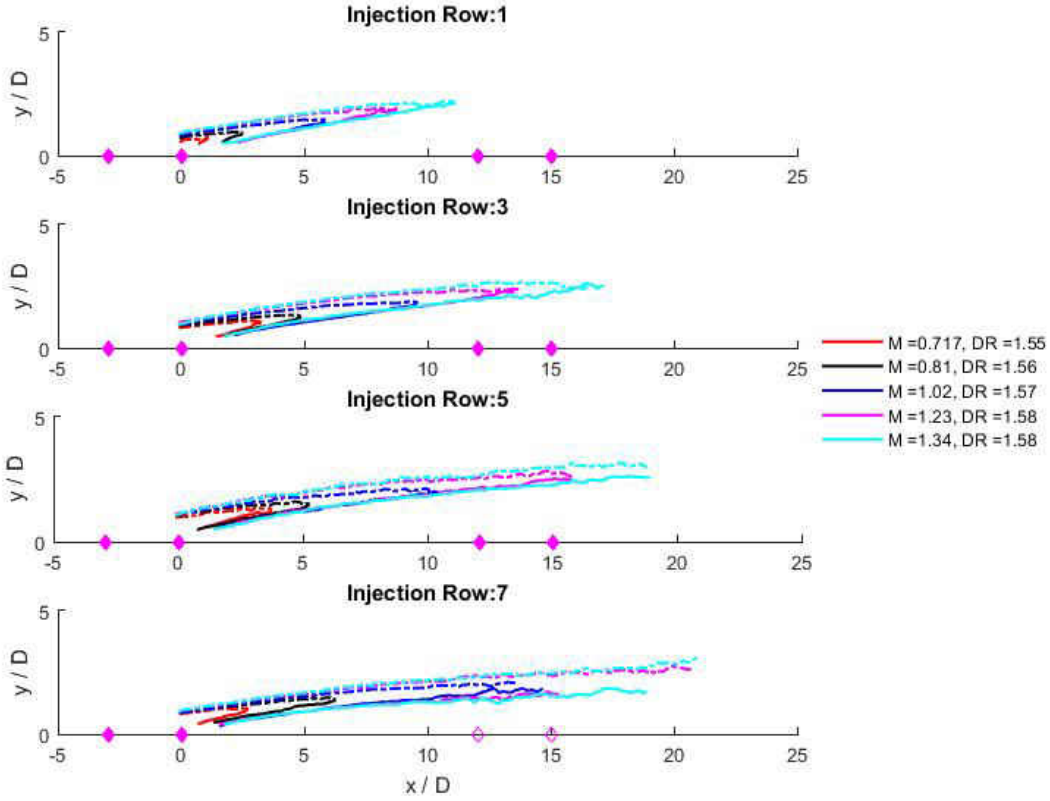

Figure 3.29: Jet trajectory per row of injection per blowing ratio for CO_2

When observing the trends of the centerline trajectory, the third and fifth row of injection can be seen to have a roughly consistent downstream path irregardless of blowing ratio (represented by the solid line in figure 3.28 and figure 3.29). Alternatively, the trajectory of the first and seventh rows of injection appears to have a greater sensitivity to changes in blowing ratio.

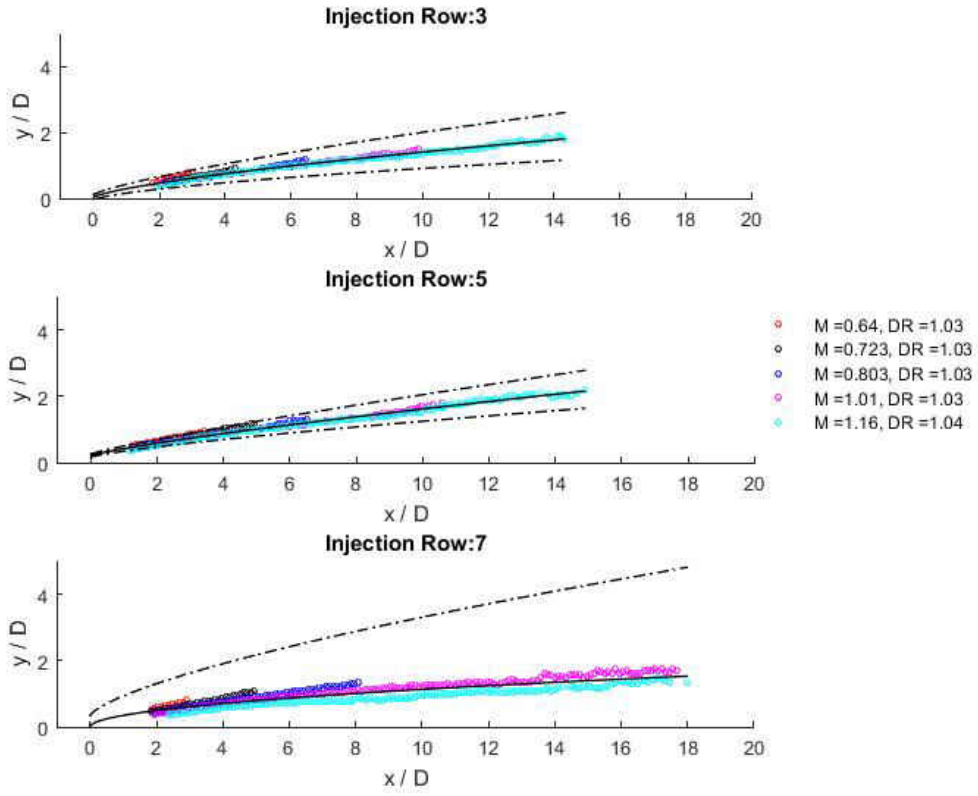

Figure 3.30: Curve fit for third, fifth, and seventh rows of injection for Air

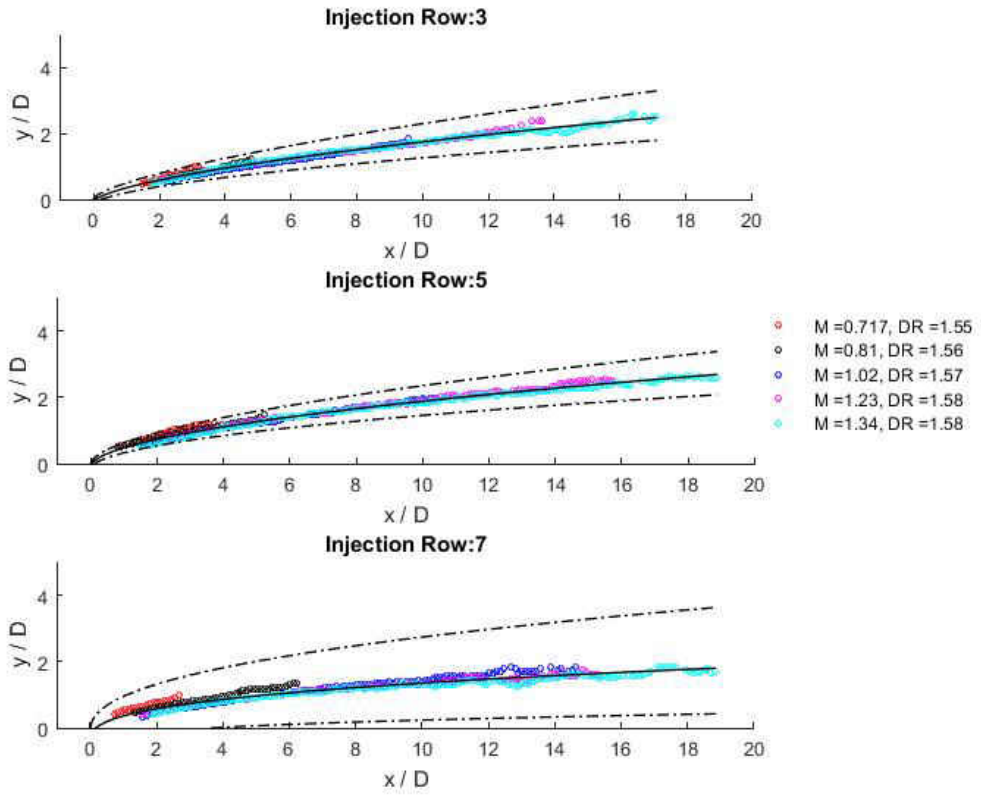

Figure 3.31: Curve fit for third, fifth, and seventh rows of injection for CO_2

The results of the centerline trajectory for the third, fifth, and seventh rows of injection for use of air and CO_2 are displayed in figure 3.30 and figure 3.31, respectively. The resulting downstream centerline trajectories are then curve fit using a power function of the form $Ax^B + C$ for both each row of injection using both air and CO_2 as the coolant. Within these figures, the resulting curve fit for each row and coolant type is represented by the solid black line. The dashed black lines within each figure represents the upper and low bounds of the 95% confidence interval

when curve fitting the centerline trajectory. The resulting constants obtained from the curve fit are shown in table 3.5. Note, while the centerline trajectory for the seventh row has shown to be more sensitive to changes in blowing ratio, the constants for the curve fit are still provided for completeness of work.

Table 3.5: Trajectory curve fitting coefficients

		$y = Ax^B + C$			
Row Number	Gas	A	B	C	R^2
Row 3	Air	0.27	0.70	0.02	0.985
Row 5	Air	0.22	0.81	0.21	0.985
Row 7	Air	0.35	0.51	0.004	0.804
Row 3	CO_2	0.42	0.63	-0.07	0.988
Row 5	CO_2	0.57	0.54	-0.09	0.988
Row 7	CO_2	0.79	0.35	-0.42	0.927

The resulting curve fits for the third, fifth, and seventh rows of injection for both air and CO_2 are shown in figure 3.32. For reference, the solid line within the figure represents the air results while the dashed line represents that of the CO_2.

The higher density CO_2 injection has an elevated wall normal presence and extends further downstream than that of the air injection, seen in figure 3.32. Additionally, both the wall normal location and downstream influence increase from the third to the fifth row of injection for both Air and CO_2. The suggestion that the centerline trajectory for CO_2 occurs at a higher wall normal height than that of Air is a suprising result. Consider the constant blowing (mass-flux) ratio comparison for the injection of Air versus CO_2. The derivation below confirms that the injection of CO_2 occurs at a velocity $\frac{2}{3}$ of the injection of Air.

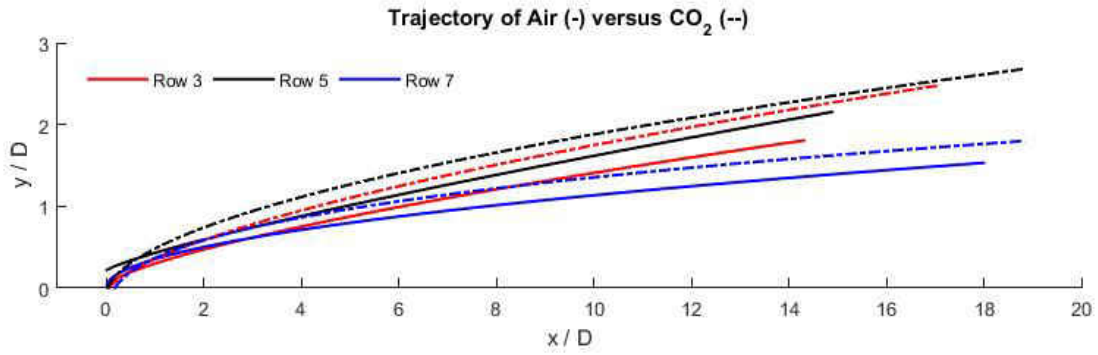

Figure 3.32: Curve fit for third, fifth, and seventh rows of injection: Air versus CO_2

$$M_{Air} = M_{CO2} \Rightarrow \frac{(V * DR)_{Air}}{(V * DR)_{CO2}} = 1 \tag{3.1}$$

$$(\frac{u_{c_{Air}}}{u_{c_{CO2}}}) * (\frac{DR_{Air}}{DR_{CO2}}) = 1 \Rightarrow (\frac{2}{3}) u_{c_{Air}} = u_{c_{CO2}} \tag{3.2}$$

While it is shown that the injection of CO_2 occurs at a slower velocity than that of Air, the results seen in figure 3.32 suggests the the injection of the faster moving fluid remains closer to the wall, while the higher density ratio seems to experience a greater jetting effect. It is believe that due to the similarity in density between the coolant and freestream that the injection of Air enters the boundary layer less perturbed, and thereby is able to remain closer to the target surface. Further investigation is needed to fully support this hypothesis.

When observing the transition from the fifth to the seventh row of injection, a dramatic

decrease in wall normal height can seen from the jet issuing from the seventh row in figure 3.32. It is believed that the low velocity stagnation region produced on the upstream edge of the hole due to the injection of the coolant into the boundary layer produces a local high pressure region thus influencing the trajectory of the previous row away from the wall. Such hypotheses are made due to the elevated wall normal height of the trajectory for both the third and fifth row where there exists an injections downstream of each of these rows. However, in the case of the seventh row of injection where there exists no influence of a preceding downstream injection, the trajectory of the seventh row is observed to remain significantly closer to the wall.

3.3 Pressure Gradient Calculations

The ability to determine the pressure throughout an entire field presents a challenge. Modern measurement techniques such as pitot-static and five-hole probes are intrusive and can change the overall flowfield upon insertion. Additionally, these mentioned techniques are limited near the wall, specifically for five-hole probe, as the calibration performed on such a probe is done at freestream conditions making near wall measurements erroneous.

By using the x and y momentum components of the Reynolds Averaged Navier Stokes equations (RANS) along with velocity data obtained from PIV, the pressure gradient field can be calculated [22], [23], [24]. However, since only 2D PIV was used during testing, the out-of-plane velocity component is unavailable for these calculations. In order to calculate the true pressure gradient field, all three components of velocity would be required. While the calculation of the pressure gradient using only two components provides an approximation, the third component can be neglected if the two components used are the dominating terms. Since the data is captured at the centerline plane of injection, where the out-of-plane contribution to pressure is minimal, the two component approximation of the pressure gradient proves to be sufficient [24].

The x and y momentum equations are re-arranged such that the pressure gradient term is located on the left hand side and the resulting right hand side can be determined from the velocity data obtained from PIV, seen in equation 3.3 and equation 3.4. The MatLAB gradient function ***gradient*** was used to preform the gradient calculations. Within these equations, density and dynamic viscosity are taken to be constant. Complications arise when injecting with CO_2 as there are variations in both density and viscosity between the injecting fluid and the boundary layer. In order to eliminate possible errors with non-similar gases, the pressure gradient field is solved and displayed only for the air injection cases.

$$\frac{dP}{dx} = -\rho(u\frac{du}{dx} + v\frac{du}{dy} + \frac{d\overline{uu}}{dx} + \frac{d\overline{uv}}{dy}) + \mu\nabla^2 u \tag{3.3}$$

$$\frac{dP}{dy} = -\rho(u\frac{dv}{dx} + v\frac{dv}{dy} + \frac{d\overline{uv}}{dx} + \frac{d\overline{vv}}{dy}) + \mu\nabla^2 v \tag{3.4}$$

The calculated pressure gradient field as a results of solving equation 3.3 and equation 3.4 can be seen in figure 3.33 and figure 3.34. The pressure gradient field is represented by the quiver displayed in these figures. Additionally, streamlines are inserted at each row of injection at a height of 0.52D from the wall, and located at -2.92D, 0D, and 2.92D relative to the downstream edge of the hole. For reference, the data displayed in figure 3.33 and figure 3.34 has a blowing ratio of M = 1.45 and a density ratio DR = 1.04.

A re-circulatory region can be seen near the upstream edge of a row in figure 3.33 and figure 3.34. This re-circulatory region can be associated with the low velocity stagnation region produced by the injection of coolant into the boundary layer. When observing the path of the streamlines, it can

When observing the path of the streamlines when interacting with this stagnation region, it is seen that the presences of this high pressure region influences the streamlines away from the wall and further into the boundary layer. However, when observing the interaction where the fifth row of injection would be found, no such stagnation region exists. With the lack of injection, there exists no such high pressure leading edge region and the jet is thereby remains closer to the wall.

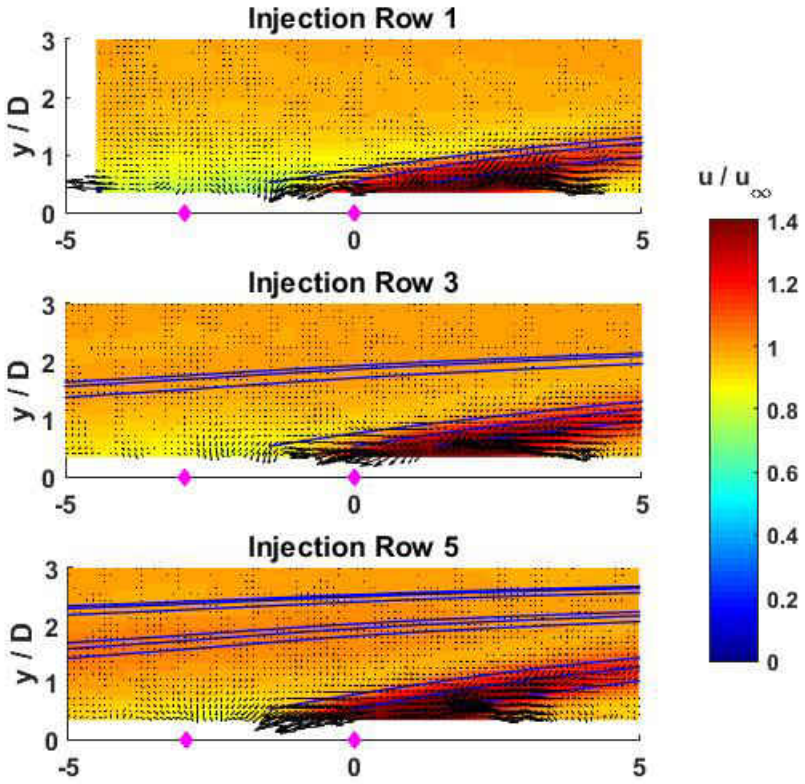

Figure 3.33: Pressure gradient field for row 1 through row 3

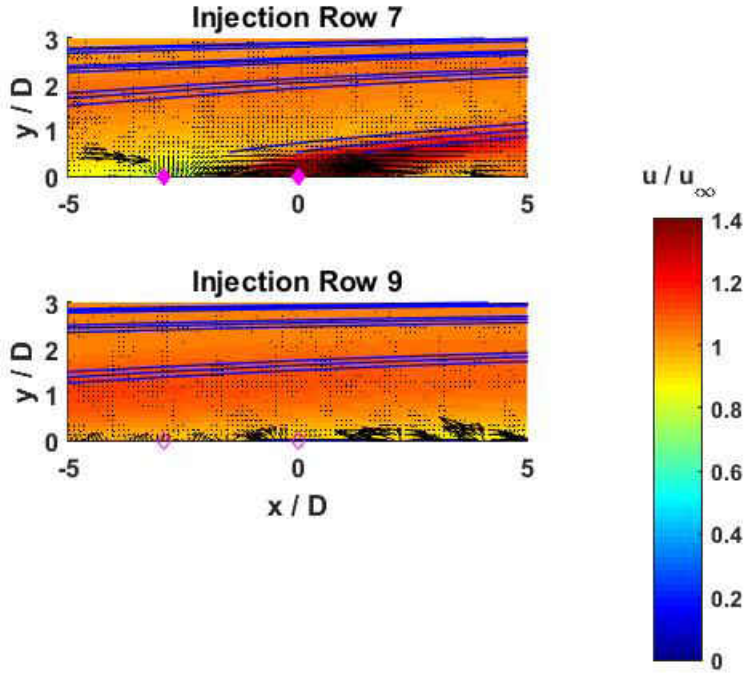

Figure 3.34: Pressure gradient field for row 4 and row 5

3.4 Momentum Thickness

Momentum thickness is defined as the vertical distance the wall should be displaced to account for the reduced momentum due to the influence of the boundary layer, and is defined mathematically in equation 3.5. Based on the derivation of momentum thickness, positive contributions to momentum thickness are seen when $u < u_\infty$ as there exists a deficit in velocity from that of the freestream. However, negative contributions to momentum thickness are observed when the local velocity is

greater than that of the freestream such that $\frac{u}{u_\infty} > 1$.

$$\theta = \int_0^{y\to\infty} \frac{u}{u_\infty}\left(1 - \frac{u}{u_\infty}\right)dy \tag{3.5}$$

In a typical flat plate boundary layer with no injection, the highest velocity seen at a given downstream location would be the freestream velocity. As such, the contribution to the momentum thickness for each local velocity would be positive. However the introduction of the secondary flow through the discrete film cooling holes presents the opportunity for a negative influence in momentum thickness. The wall normal velocity profile for the blowing ratio M = 1.16 with a density ratio DR = 1.04 at a downstream location of x/D = 3.56 is displayed in figure 3.35. The red line within this figure represents the streamwise velocity profile at this given downstream location, where the green line represents the contribution to momentum thickness. Additionally, figure 3.36 shows the centerline contour plot displaying streamwise velocity, where the black line shows the location of the velocity profile shown in figure 3.35.

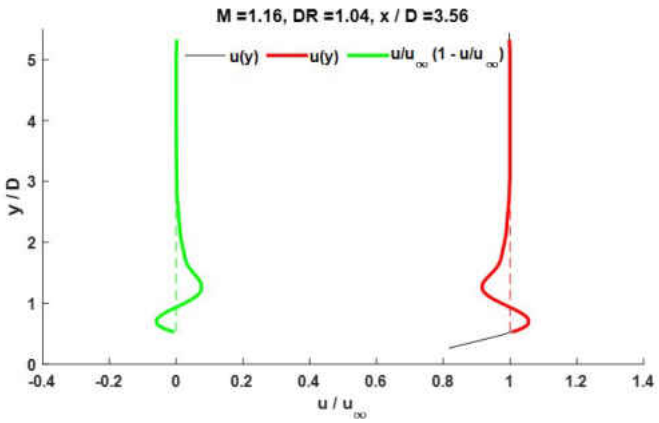

Figure 3.35: Wall normal velocity profile and momentum thickness calculation

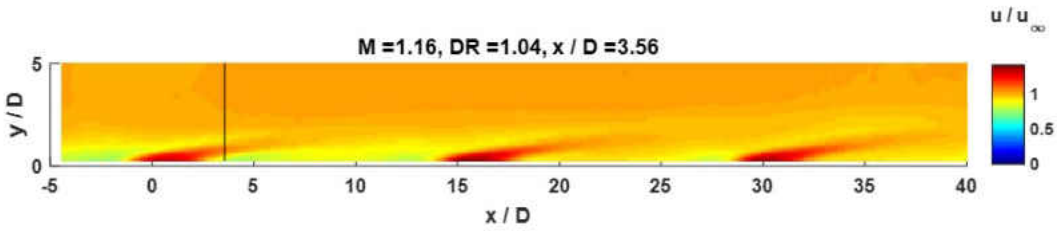

Figure 3.36: Streamwise velocity contour displaying velocity profile location

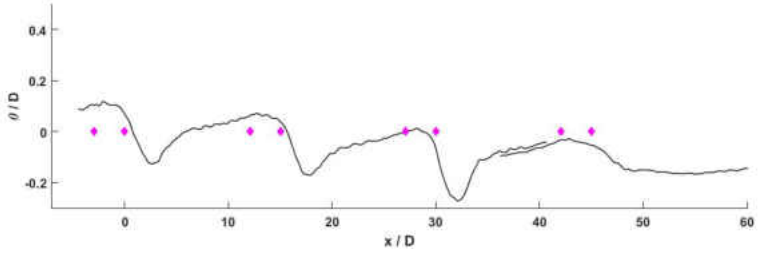

Figure 3.37: Momentum thickness calculation for M = 1.16 with DR = 1.04

With the injection of the high velocity secondary fluid into the boundary layer there exists a portion of the velocity profile where $\frac{u}{u_\infty} > 1$, as seen in figure 3.35. This elevated local velocity contributes negatively to momentum thickness as there is a surplus of momentum when compared to that of the freestream. The momentum thickness is thereby reduced in wall normal magnitude in the downstream locations where there exists local velocity magnitudes greater than that of the freestream. The calculated momentum thickness for the blowing ratio M = 1.16 test with a density ratio DR = 1.04 is displayed in figure 3.37. Recall that the magenta diamonds represent the x/D

location of the leading and trailing edge of injection hole for each row.

As discussed earlier, the availability of data in the near wall region was affected by reflections present due to the testing technique used. The amount of data lost varied slightly throughout the entire test matrix, resulting is a variation in the wall normal location of the lowest data point. In order to maintain continuity in terms of available data when calculating the momentum thickness, an offset was used when evaluating the lower limit of the momentum thickness integral seen in equation 3.5. While the equation call for the lower limit to be evaluated at y = 0, the resulting calculations were preformed with a lower limit of 0.52D. Similar to the numerical procedure used when searching for the jet trajectory, the streamwise velocity profile was curve fit using a cubic interpolator per downstream location. The curve fit was then evaluated with a resolution of 0.0001 mm.

The black line seen in figure 3.35 represents the velocity profile plotted with the entire data available at this given downstream location. The red line represents the same velocity profile but can be seen to exclude the data below y/d = 0.52, and represents the data used to calculate the momentum thickness at this given downstream location.

A comparison of the resulting momentum thickness when using the wall normal offset to using the entire data available per downstream location is made in figure 3.38 and figure 3.39. For reference, this comparison is made using the blowing ratio M = 1.16 with a density ratio of DR = 1.04. As a result, it can be seen that the trend and overall magnitude of momentum thickness per downstream location does not appreciably deviate when using a wall normal offset. At the downstream location of x/d = 3.56 the difference in momentum thickness when using the wall normal offset versus the entire available data is 0.1% of a hole diameter.

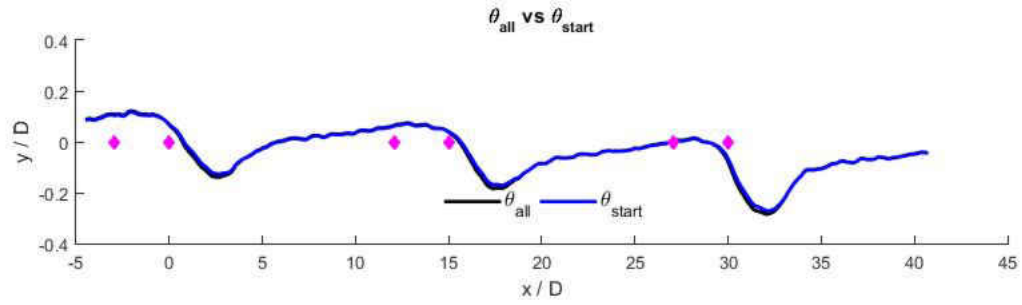

Figure 3.38: Example of momentum thickness calculation with and without starting wall normal offset

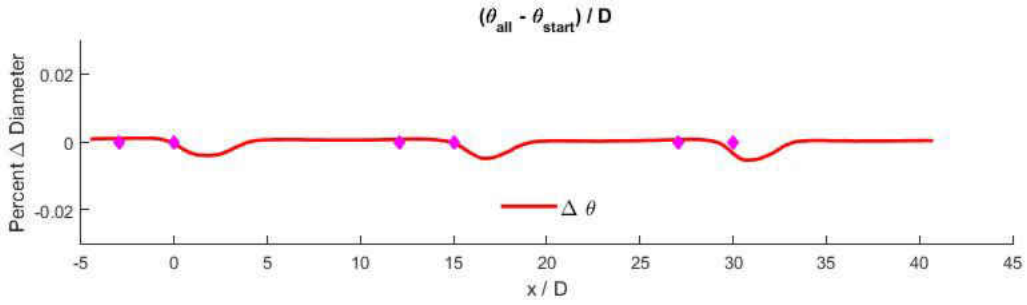

Figure 3.39: Example of percent difference between momentum thickness calculation with and without starting wall normal offset

3.4.1 Momentum Thickness Results

The resulting downstream momentum thickness calculations for the injection of air can be seen in figure 3.41. When observing the trends for the injection of air, the relative downstream momentum thickness remains relatively constant for the blowing ratios M = 0.397 to M = 0.803. As the blowing ratio increases above M = 0.803, a rapid decrease in momentum thickness is observed

throughout the boundary layer. The dramatic decreases in momentum thickness is observed for the elevated blowing ratios is due to the local velocity magnitude being greater than that of the freestream. These negative contributions to momentum thickness are mainly seen in the immediate downstream region of a row of injection, where the jet velocity is greatest prior to diffusing with the boundary layer.

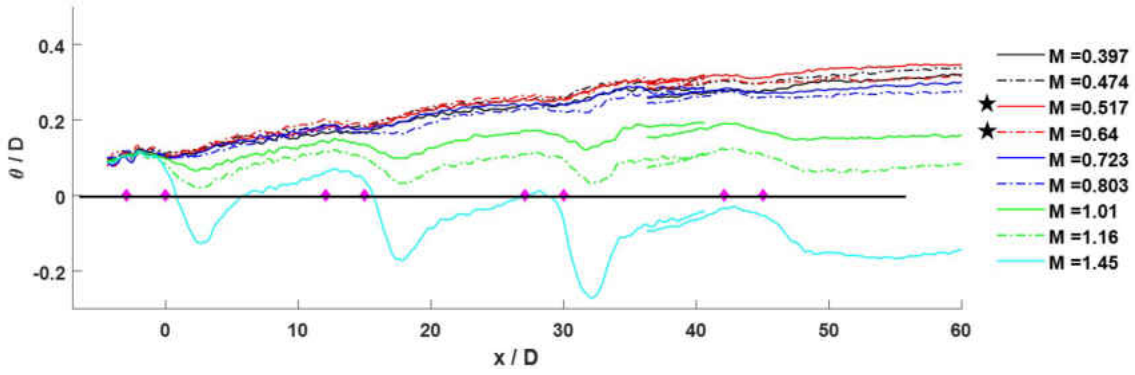

Figure 3.40: Momentum thickness for the injection of Air

In order to more thoroughly classify the relationship between blowing ratios and the resulting momentum thickness, the average momentum thickness is calculated downstream of each row of injection for each blowing ratio. These averages are calculated using the available data between the trailing edge for a given row of holes and the upstream edge of the preceding downstream row of holes. The results from the average momentum thickness calculations are displayed in figure 3.41.

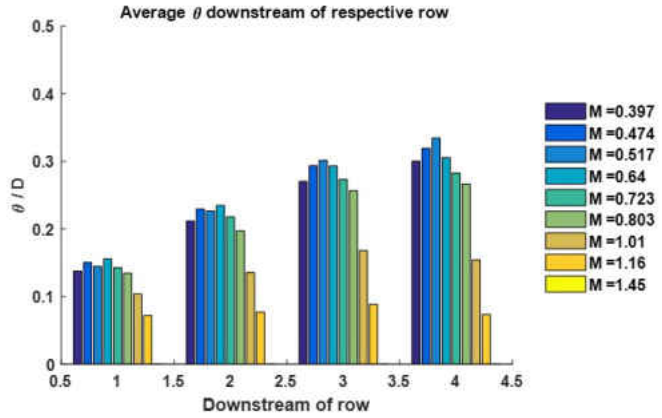

Figure 3.41: Average downstream momentum thickness for the injection of Air

As expected from the observed trends in downstream momentum thickness, the average momentum thickness downstream of a row of holes for the blowing ratios between M = 0.397 and M = 0.803 are similar in magnitude. For the highest blowing ratio M = 1.45, the average momentum thickness downstream of each row of injection is observed to be negative. This suggests that the resulting wall displacement would be downwards due to the surplus of momentum in the boundary layer upon injection of the high velocity coolant.

CHAPTER 4: CONCLUSIONS

New designs of increased film cooling performance are developed consistently. The ability to test the performance of a proposed film cooling configuration at typical engine-like conditions is dependent on the capabilities available during the time of testing and the technique implemented. While density ratios observed at engine-like conditions vary between 1 and 2.5, the majority of the available literature evaluates film cooling performance at density ratios between 1 and 1.5. Its imperative to confidently determine that the film cooling performance evaluated at a density ratio outside of engine-like conditions will accurately scale to the density ratio range expected at engine-like conditions.

Particle image velocimetry is used to capture the spatially resolved flow field produced by the interaction of the boundary layer and a stagger arrangement of eight film cooling rows, containing a total of 52 holes. A simple cylindrical and fan-shape film cooling configuration are each evaluate in the present study. Effects of density ratio on the flow field are determined by altering the density of the secondary fluid whilst independently holding either blowing, momentum flux, or velocity ratio constant.

4.1 Streamwise Velocity Contours

Streamwise velocity contours show that similarities are most apparent in jet structure for varying density ratios when blowing ratio is held constant, followed by momentum flux ratio. The initial velocity of the jet core for the lifted off cases was seen to be higher for the lower density ratio comparisons at constant blowing ratio. However, the relative length and wall normal position of the penetration for both density ratios jets was closely matched for the constant M comparisons.

Constant momentum flux ratio shows strong agreement in the velocity of the jet core for lifted off cases, however the penetration of the lower density jet into the boundary layer diffuses quicker (in terms of downstream location) than that of the higher density ratio. Constant velocity ratio in actuality can be seen to produce large differences in velocity magnitudes of the jet issuing from the film cooling configuration. The higher density injections through the cylindrical configurations for constant velocity ratios consistently are issuing into the boundary layer at noticeably higher velocities than that of the lower density ratio cases.

4.2 Jet Trajectory Tracking

By tracking the centerline trajectory and the upper bound limit of the jet as interacts with the boundary layer, a better understanding of the overall downstream influence was obtained. When comparing the length of interaction per blowing ratio per row of injection, it was observed that the convergence between the centerline and upper bound of the jet occurred in the vicinity of the upstream edge of the preceding row of injection.

The resulting centerline trajectories downstream of the third, fifth, and seventh row of injection remained relatively insensitive to changes in blowing ratio. As such, these centerline trajectories are then curve fit using a power function for each row of injection for both air and CO_2. It is observed from the corresponding curve-fitting that the centerline trajectory for the injection of CO_2 extends further downstream and sustains a greater wall normal elevation than that of the similar air injection. When comparing the trajectories between the third and fifth rows of injections, it is observed that the wall normal influence of the jet increases from the third to the fifth row. However, when observing the seventh row of injection where there exists no influences of a preceding row, the resulting centerline trajectory remains closer to the wall.

4.3 Pressure Gradient

Using the x and y components of momentum from the RANS equations, the pressure gradient field was calculated, and showed a high pressure re-circulatory region upstream of a row of injection. The re-circulatory region upstream of a row of injection is associated with the stagnation region as a result of the blockage produced by the injection of high velocity coolant into the boundary layer. By examining the interaction between streamlines produced within the jet and this re-circulatory region, it was observed that the stagnation region influenced the jet away from the surface. It is believed that the lack of a ninth row of injection, where a high pressure re-circulatory region would exist, allows the injected coolant to remain closer to the target surface. While the results found by examining the pressure gradient calculations support the findings in tracking the trajectory of the jet, continued investigations are required to further justify this hypothesis.

4.4 Momentum Thickness

The momentum thickness is calculated for each case per downstream location. Relatively constant momentum thickness is observed for the injection of the lower density ratio through the cylindrical configuration for the blowing ratio range M = 0.4 to M = 0.8. As the blowing ratio continued to increase, negative influences in momentum thickness were observed as the local streamwise velocity magnitude became greater than that of the freestream. The results from these elevated local velocities suggest that the displacement of the wall should occur in the downward direction due to the surplus of momentum in the boundary layer by the injection of the coolant.

By calculating the average momentum thickness between rows of injection, a more definite conclusion of the maximum momentum thickness for a given set of blowing ratios can be determined. Based on the results from these calculations, the maximum average downstream mo-

mentum thickness occurs at a blowing ratio of M = 0.52.

Based on the research performed in this study, it is postulated that the peak in average downstream momentum thickness corresponds well with film cooling performance. When momentum thickness is greatest, there is a large coverage of slow moving fluid in the near wall shielding the target surface from the fast moving hot freestream. As the blowing ratio increases past the peak in average momentum thickness, the injected coolant entrains more of the freestream due to jet detachment thereby increasing in temperature and streamwise velocity resulting in a decreased momentum thickness. A study performed using PSP by Natsui [25] showed that the maximum average downstream surface effectiveness for the injection of CO_2 through the cylindrical configuration occurred at a blowing ratio of M = 0.44. In order to verify this theory, future work can be done by the injection of nitrogen while using pressure sensitive paint (PSP) to simulate a density ratio of approximately 1.

LIST OF REFERENCES

[1] R. S. Bunker, *The Gas Turbine Handbook*, ch. 4.2.1 Cooling Design Analysis. National Energy Technology Laboratory, 2006.

[2] R. S. Bunker, "A review of shaped hole turbine film cooling technology," *Journal of Heat Transfer*, 2005.

[3] T. Kampe, S. Volker, and F. Zehe, "A model for cylindrical hole film cooling - part 1: A correlation for jet-flow with application to film cooling," *Journal of Turbomachinery*, 2012.

[4] M. K. Eberly and K. A. Thole, "Time-resolved film-cooling flows at high and low density ratios," *Journal of Turbomachinery*, 2013.

[5] J. R. Pietrzyk, D. G. Bogard, and M. E. Crawford, "Effects of density ratio on the hydrodynamics of film cooling," *Journal of Turbomachinery*, 1990.

[6] J. Hossain, L. V. Tran, J. S. Kapat, E. Fernandez, and R. Kumar, "Flow and heat transfer analysis in a single row narrow impingement channel: Comparison of piv, les, and rans to identify rans limitations," in *Turbomachinery Technical Conference & Exposition*, 2014.

[7] J. Hossain, E. Fernandez, C. Garrett, and J. Kapat, "Flow and heat transfer analysis in a single row narrow impingement channel: Comparison of piv, les, and rans to identify rans limitations," in *Turbomachinery Technical Conference & Exposition*, 2017.

[8] R. J. Goldstein and E. R. G. Eckert, "Effects of hole geometry and density on three-dimensional film cooling," *Journal of Heat and Mass Transfer*, 1974.

[9] S. Bernsdorf, M. G. Rose, and R. S. Abhari, "Modeling of film cooling - part 1: Experimental study of flow structure," *Journal of Turbomachinery*, 2006.

[10] B. Johnson, K. Zhang, W. Tian, and H. Hu, "An experimental study of film cooling effectiveness by using piv and psp," in *American Institute of Aeronautics and Astronautics*, 2013.

[11] P. Schreivogel, B. Kross, and M. Pfitzner, "Density ratio effects on the flow field emanating from cylindrical effusion and trenched film cooling holes," in *The American Society of Mechanical Engineers*, 2014.

[12] M. K. Eberly and K. A. Thole, "Time - resolved film cooling flows at high and low density ratios," *Journal of Turbomachinery*, 2014.

[13] T. B. Watson, S. N. Toudeshki, L. M. Wright, D. C. Crites, M. C. Morris, and A. Riahi, "Application of s-piv for investigation of round and shaped film cooling holes at high density ratios," in *American Society of Mechanical Engineers*, 2016.

[14] M. K. Harrington, M. A. McWaters, D. G. Bogard, C. A. Lemmon, and K. A. Thole, "Full-coverage film cooling with short normal injection holes," in *American Society of Mechanical Engineers*, 2001.

[15] W. Jessen, M. Konopka, and W. Schroeder, "Particle - image velocimetry measurements of film cooling in an adverse pressure gradient," *Journal of Turbomachinery*, 2012.

[16] R. J. Adrian and J. Westerweel., *Particle Image Velocimetry*. ew York: Cambridge University Press, 2001.

[17] *OIL DROPLET GENERATORS MODELS 9307 AND 9307-6*.

[18] H. Tennekes and J. L. Lumley, *A first course in turbulence*. The MIT Press, 1972.

[19] A. Melling, "Tracer particles and seeding for particle image velocimetry," *Measurement Science and Technology*, 1997.

[20] M. Samimy and S. Lele, "Motion of particles with inerita in a compressible free shear layer," *American Institute of Physics*, 1991.

[21] J. Nogueira, A. Lecuona, and P. A. Rodriguez, "Data valiadation, false vectors correction and derived magnitudes calculation on piv data," *Measurement Science and Technology*, 1997.

[22] E. Roosenboom, "Experimental analysis of the flow around a cylinder with a square cross-section," Master's thesis, Delft University of Technology, 2003.

[23] B. van Oudheusden, F. Scarano, E. Roosenboom, E. Casimiri, and L. Souverdein, "Evaluation of intergral forces and pressure fields from planar velocimetry data for incompressible and compressible flows," *Experiments in fluids*, 2007.

[24] E. Fernandez, *On the properties and mechanisms of microjet arrays in crpssflow for the control of flow separation*. PhD thesis, Florida State University, 2014.

[25] G. Natsui, *Multi-row Film Cooling Boundary Layer*. PhD thesis, University of Central Florida, 2015.